EES Catalysis

REVIEW ARTICLE

View Article Online
View Journal

Cite this: DOI: 10.1039/d5ey00314h

Harnessing chirality in nanomaterials: advancing photocatalysis for hydrogen production and beyond

Nur Aqlili Riana Che Mohamad, [a] Dong-Il Won,[a] Haeun Kang,[a] Jeongwon Kim, [a] Kyunghee Chae, [a] Minju Kim, [b] Mingyue Zhang,[b] Zhiqun Lin *[b] and Dong Ha Kim *[acd]

Received 1st November 2025,
Accepted 19th January 2026

DOI: 10.1039/d5ey00314h

rsc.li/eescatalysis

Solar-driven chemical conversion stands as a basis strategy for realizing sustainable energy technologies. Within this context, chiral photocatalysts have emerged as a new generation of materials that unify light–matter interactions with asymmetric molecular recognition. The integration of chirality into nanostructured systems introduces inherent structural and electronic asymmetry, enhancing light absorption, chiroptical activity and charge carrier dynamics. The cooperative effects collectively improve photocatalytic efficiency, particularly in solar-driven hydrogen evolution. In parallel, the chiral-induced spin selectivity (CISS) effect promotes spin-polarized charge transport, accelerates reaction kinetics and refines product selectivity. This review elucidates the mechanistic origins of chirality in catalyst design, encompassing molecular interactions, light-mediated induction and template-assisted synthesis. It evaluates recent advances in the characterization and construction of multiclass chiral photocatalysts, with emphasis on hydrogen evolution, alongside extensions to photocatalytic CO_2, N_2 reduction and other emerging reaction paradigms. The outlook presented herein underscores emerging opportunities for rationally designing chirality-driven photocatalysts as a transformative platform for next-generation solar-to-chemical energy conversion.

Broader context

Achieving net-zero emissions demands catalytic platforms capable of converting solar energy into storable chemical fuels with greater efficiency and selectivity. Photocatalysis remains central to this vision, yet limitations in light harvesting, charge carrier management and control over multi-electron pathways continue to restrict practical performance. Within this context, chirality is emerging as a promising and relatively untapped dimension in photocatalyst design. Introducing chirality into photocatalytic materials imparts structural and electronic asymmetry that influences how light is absorbed and how charge carriers are generated, separated and utilized at interfaces. The asymmetry enriches light–matter and chiroptical interactions, offering new opportunities to guide reaction selectivity. The increasing recognition of the CISS effect further underscores the potential of spin-polarized charge transport to modulate interfacial reaction dynamics, particularly for solar-driven hydrogen evolution and other multi-electron transformations such as CO_2 and N_2 reduction. Looking ahead, progress will rely on strengthening the mechanistic understanding of how chirality is introduced, transferred and maintained within diverse photocatalytic architectures, and how spin and interfacial chemistry can be co-engineered. Advancing this knowledge may pave the way for scalable, chirality-guided photocatalysts that support next-generation solar-to-chemical energy technologies.

Introduction

The efficient conversion of solar energy into chemical fuels through photochemical processes represents a pivotal strategy for addressing global energy and environmental challenges. Among these, photocatalytic water splitting has attracted particular attention due to the natural abundance of sunlight and water, combined with the high gravimetric energy density of hydrogen (33.3 kWh kg^{-1}), positioning it as a clean and sustainable energy carrier.[1–5] Despite substantial progress, the

[a] Department of Chemistry and Nanoscience, Ewha Womans University, 52 Ewhayeodae-gil, Seodaemun-gu, Seoul 03760, Republic of Korea. E-mail: dhkim@ewha.ac.kr
[b] Department of Chemical and Biomolecular Engineering, National University of Singapore, Singapore 117585, Singapore
[c] Institute for Multiscale Matter and Systems, Ewha Womans University, 52 Ewhayeodae-gil, Seodaemun-gu, Seoul 03760, Republic of Korea
[d] Basic Sciences Research Institute (Priority Research Institute), Ewha Womans University, 52 Ewhayeodae-gil, Seodaemun-gu, Seoul 03760, Republic of Korea

large-scale implementation of photocatalytic systems remains constrained by low conversion efficiency, sluggish charge carrier dynamics and poor product selectivity. Moreover, noble-metal chiral plasmonic systems (*e.g.*, Au and Pt) remain indispensable for elucidating light–matter interactions, however, their complex synthesis and high cost restrict scalability and economic viability. This gap motivates the development of earth-abundant chiral photocatalysts that preserve performance gains while minimizing reliance on noble metals. In recent years, the incorporation of chirality into photocatalytic materials has emerged as a transformative approach to overcoming these intrinsic limitations.[6–8] Chirality, a geometric property describing the non-superimposability of a structure with its mirror image profoundly influences the optical, electronic and catalytic behavior of nanomaterials. At the nanoscale, chiral catalyst architectures can modulate light–matter interactions, direct spin-polarized charge transport through the CISS effect and establish selective interactions with molecular reactants.[6,9,10] Collectively, these features enhance charge separation and transport, enable spin-dependent surface redox processes and promote selective reaction pathways.

This review highlights recent advances in chiral photocatalysis, emphasizing the mechanistic principles that govern chirality induction, light–matter interactions and their collective impact on catalytic performance (Fig. 1). We discuss rational design strategies for chiral nanostructures, various approaches for inducing and characterizing chirality at the nanoscale and the implications of chirality in photo(electro)catalytic reaction dynamics. Beyond water splitting, we also explore its emerging roles in carbon dioxide reduction reaction (CO_2RR) and nitrogen reduction reaction (N_2RR), where stereoelectronic and spin-selective effects may open new mechanistic pathways and enhance product selectivity.

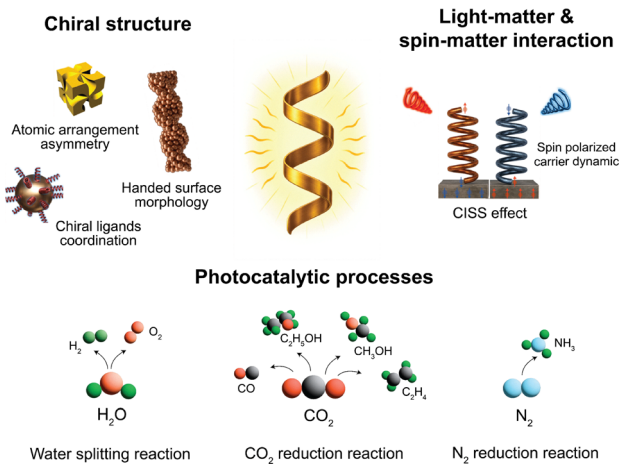

Fig. 1 Schematic overview illustrating how chirality governs light–matter and spin–matter interactions at photocatalytic interfaces. Chiral geometries modulate circularly polarized light absorption and spin-polarized charge dynamics, enabling selective and efficient photocatalytic transformations for solar-driven hydrogen production and beyond.

Chirality in catalyst design

Chirality introduces a new dimension of functionality in catalyst nanomaterials, imparting distinctive physical, electronic and chiroptical properties that can significantly enhance photocatalytic performance. The non-superimposable structural nature of chiral systems influences key parameters such as charge carrier mobility, photoconductivity and surface electronic states, depending on how chiral molecular orientations or chiral templates interact with the nanomaterial framework.[11–14] In this context, chirality in nanomaterials can be induced *via* three principal pathways: (i) chirality induction through molecular interactions, (ii) light-mediated chirality and (iii) template-assisted approaches. The following section focuses on the first pathway, which encompasses the direct induction of chirality through molecular-level interactions with chiral organic species.

Chirality induction through molecular interactions

Chiral molecules such as amino acids, polypeptides and proteins play a pivotal role in directing the nucleation, growth and morphology of nanomaterials by functioning as surface ligands, stabilizers or structure-directing agents.[15,16] Molecular-level asymmetry derived from these interactions serves as the foundation for the emergence of chiral nanostructures, influencing their optical activity, charge transport and catalytic behavior. Common chiral molecules such as cysteine, glutathione and tartaric acid are widely employed owing to their affordability, availability and strong affinity for metal surfaces, making them effective mediators of chirality transfer in nanomaterial synthesis.[17,18] The interactions between chiral molecules and inorganic surfaces can trigger diverse responses including surface reconstruction, ligand coordination and adsorption, covalent and non-covalent bonding and phase transitions that collectively mediate the incorporation of molecular chirality into inorganic frameworks.

Surface reconstruction. Chiral organic molecules can drive surface reconstruction on inorganic nanomaterials, transferring their stereochemical information to the atomic arrangement of the surface. Acting as surface ligands, these molecules interact asymmetrically with metal atoms, inducing the reorganization of surface coordination sites and breaking mirror symmetry at the interface. This process establishes the foundation for atomic-scale chirality and enables the enantioselective evolution of nanostructures. For instance, Yao *et al.* demonstrated that D-/L-penicillamine ligands direct the formation of enantiomeric Au nanoclusters, where asymmetric coordination through thiol and amine functionalities induces mirror-image atomic configurations and distinct circular dichroism (CD) responses.[19] Similarly, Yang *et al.* achieved enantioselective synthesis of Ag nanoclusters using chiral diphosphine ligands, revealing that precise ligand coordination can reorganize surface atoms into chiral motifs.[20] Comparable behavior has been observed in semiconductor nanocrystals, where D/L-cysteine molecules induce S-/R-type surface configurations in CdTe nanocrystals,[21] while penicillamine-capped CdS nanocrystals

form chiral shells surrounding otherwise achiral cores.[22] These findings collectively underscore that the stereochemistry and binding mode of surface ligands govern atomic coordination and reconstruction at the organic–inorganic interface, establishing a decisive link between molecular asymmetry and nanoscale chirality.

At the mesoscale, surface reconstruction extends beyond atomic coordination to influence overall nanoparticle morphology. Lee *et al.* demonstrated that introducing chiral biomolecules during Au nanoparticle growth modulates the tilt and curvature of surface boundaries.[23] Specifically, cysteine ligands promote inward boundary tilting on cubic Au seeds, whereas glutathione molecules induce outward, pinwheel-like structures. The direction and extent of reconstruction depend sensitively on the type of chiral ligand employed, enabling the synthesis of chiral Au and Pd nanoparticles with tunable handedness and optical activity. Meanwhile, in halide-assisted differential growth, chiral ligands preferentially stabilize high-index facets while halide ions regulate facet-specific growth kinetics, producing triskelion-like nanoparticles with threefold rotational symmetry (Fig. 2).[24] Chiral surface reconstruction has also been observed in twisted inorganic nanoarchitectures. In a recent study, Tan *et al.* demonstrated a family of twisted chiral inorganic structures, including hollow Co_3O_4 and related chalcogenides using D-/L-cysteine, where controlled topological transformation generates tunable twist degrees, handedness and composition.[25]

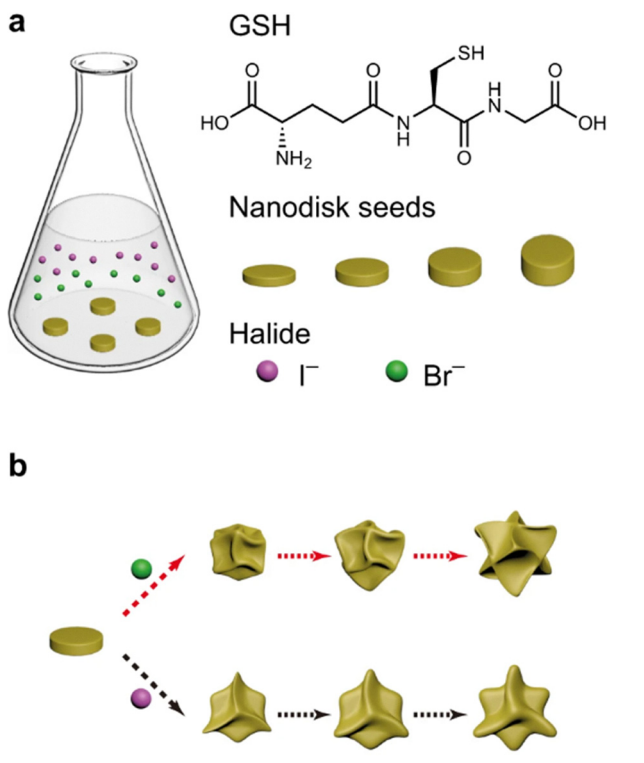

Fig. 2 (a) Schematic illustration of the synthesis of chiral Au nanocrystals *via* helicoid-assisted deposition growth (HADG). The as-prepared Au nanodisks were employed as anisotropic seeds in a growth solution containing GSH, CTAB, KI, $HAuCl_4$ and AA. (b) Representative chiral nanocrystals with diverse morphologies obtained through the HADG process. By tuning the CTAB/KI concentration ratio, the Au nanodisks evolved into chiral architectures exhibiting distinct rotational symmetries. Adapted with permission from ref. 24. Copyright 2023, Springer Nature.

Ligand coordination and asymmetric adsorption. Chiral ligands bearing functional groups such as –SH, –COOH and $–NH_2$ play a pivotal role in mediating chirality transfer to inorganic systems through direct coordination with surface metal centers. The incorporation of these chiral molecules into inorganic nanomaterials provides an efficient pathway for transmitting molecular asymmetry, most commonly realized through ligand-exchange coordination. In this mechanism, chiral ligands replace native achiral capping agents (*e.g.*, oleic acid) by forming stronger coordination bonds with surface metal atoms, thereby imprinting their stereochemical configuration at the inorganic interface.[26–28] This ligand-exchange route has been extensively applied to semiconductor systems, particularly MX-type nanoparticles (M = Cd, Zn or Cu; X = S, Se or Te), where the replacement of achiral surface ligands with enantiopure species such as D-/L-cysteine and penicillamine results in mirror-image CD spectra.[26,28–31] A prototypical example is the CdSe quantum dots (QDs) system, where ligand exchange with D-/L-cysteine induces pronounced chiroptical activity arising from orbital hybridization between the cysteine ligands and the CdSe lattice. This hybridization alters the local electronic density of states, giving rise to enantiospecific optical transitions that reflect the handedness of the coordinated ligands.[31]

Beyond conventional ligand exchange, external perturbations such as ultrasonication and thermal incubation have been shown to promote ligand binding or displacement at the nanoparticle surface, thereby enhancing the efficiency of chiral molecular adsorption.[27,32,33] These processes can induce chiroptical activity not only through the intrinsic asymmetry of the ligands but also *via* surface electronic rearrangements triggered by asymmetric molecular adsorption.[15] Ultrasonication-assisted functionalization of achiral Fe_3O_4 nanoparticles with chiral molecules, for instance, has yielded magnetically active chiral systems exhibiting spin-polarized behavior.[32] Likewise, adsorption of chiral species onto photoanodes has been shown to lower the overpotential for hydrogen evolution, highlighting the influence of chiral–surface interactions on charge transfer dynamics under photoelectrochemical conditions.[33] Collectively, these findings highlight that ligand-exchange coordination and adsorption-driven chiral modification not only imprint structural asymmetry but also modulate the electronic and spin states of inorganic materials, bridging molecular chirality and functional optoelectronic or catalytic responses.

Covalent bonding and non-covalent interactions. Chiral molecules can associate with nanoparticle surfaces through either covalent or non-covalent interactions, each imparting distinct stability and functionality to the resulting hybrid systems. Non-covalent interactions typically governed by hydrogen bonding, electrostatic interaction or π–π stacking, offers a facile approach for anchoring chiral modifiers. The physisorption, however, often suffers from limited stability under catalytic or photochemical conditions due to weak interfacial

bonding and possible desorption of ligands.[15,34] In contrast, covalent functionalization establishes robust linkages that secure chiral moieties to the nanoparticle surface, effectively stabilizing local stereochemical environments and sustaining chirality during catalytic activities.[34]

A representative example by Suzuki and colleagues showed that covalent edge modification of graphene QDs with L-/D-cysteine induces helical buckling and distinct CD signals, arising from orbital hybridization between cysteine edge groups and adjacent carbon atoms, as well as from nanoscale twisting of the graphene sheet.[35] Beyond covalent functionalization, covalent immobilization offers an integrated route to enhance the selectivity without blocking the catalytic sites. Zhou and colleagues exemplified this approach, where ferromagnetic Fe_3O_4 nanoparticles were coated with an amino acid encoded chiral polymer shell (Fe_3O_4@poly(amino acid)). This hybrid catalyst integrates magnetic responsiveness with chiral recognition, enabling efficient enantioselective catalysis through cooperative chiral-magnetic coupling.[36] Beyond single-nanoparticle modification, chiral organization can also emerge through controlled self-assembly mediated by non-covalent interparticle forces such as van der Waals, dipole–dipole or electrostatic interactions. The hierarchical assemblies can evolve into chiral superstructures including helices, twisted ribbons or toroidal morphologies with tunable geometries and collective optical activity.[15,34,37,38]

Phase transition. In a limited system, chiral molecules have been demonstrated to induce structural phase transitions in layered materials, thereby altering their electronic and catalytic properties. A representative example is the intercalation of chiral methylbenzylamine molecules into MoS_2, which disrupts the symmetry of the semiconducting 2H phase and promotes its transformation into the metastable 1T′ phase (Fig. 3).[39] This transition increases electrical conductivity and imparts metallic character to the material, leading to enhanced electrocatalytic activity. The resulting multilayer 1T′-MoS_2 intercalated with chiral molecules represents a promising platform for spin-polarized current generation in spintronic devices and for broader electrochemical applications.[39,40]

Light-mediated chirality induction

Light can act as a symmetry-breaking stimulus during the formation of chiral nanostructures. In particular, circularly polarized light (CPL) has been employed as an external chiral field to impart handedness to systems that would otherwise remain achiral. The distinct electromagnetic fields of left- and right-handed CPL interact differentially with molecular orientations, electronic transitions and in plasmonic systems, with hot-carrier generation. Such interactions bias nucleation and growth toward a preferred handedness.[41,42] For example, L-selenocystine combined with photo-irradiation directs the growth of helically-grooved gold nanoarrows (HeliGNAs), where light-driven cleavage/activation of diselenide functionality generates reactive selenyl species that steer helical self-assembly and produce strong plasmonic CD spectra (Fig. 4).[43] Similarly, chiral thiols or amino acids such as cysteine, when combined with CPL or light-mediated growth conditions, can induce chiral reconstruction of gold nanocrystals. These transformations, including the evolution from achiral seeds to trisoctahedral or rhombic-derived morphologies, demonstrate how molecular asymmetry coupled with photochemical or photothermal pathways imprints chirality into the developing lattice.[44,45] Overall, these studies reveal that CPL and related photochemical stimuli can encode stereochemical bias through mechanisms such as differential photoabsorption, photochemical cleavage and activation, plasmonic hot-carrier effects and light-modulated ligand dynamics. The resulting chiral materials exhibit distinct optical responses toward left- and right-handed CPL.[41,42]

Template-assisted chirality

Template-assisted synthesis provides a structurally guided approach for inducing chirality in inorganic and hybrid nanomaterials through the replication of pre-existing chiral

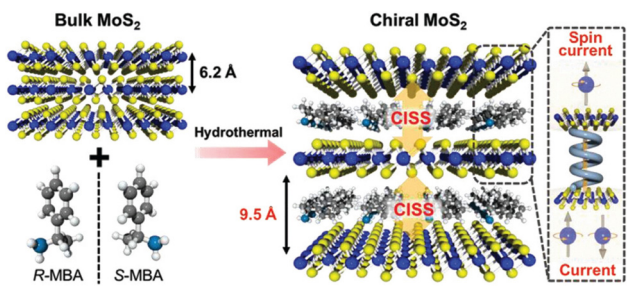

Fig. 3 Schematic illustration of chiral MoS_2 exhibiting multiple chiral-induced spin selectivity (CISS) effects. Adapted with permission from ref. 39. Copyright 2022, John Wiley and Sons.

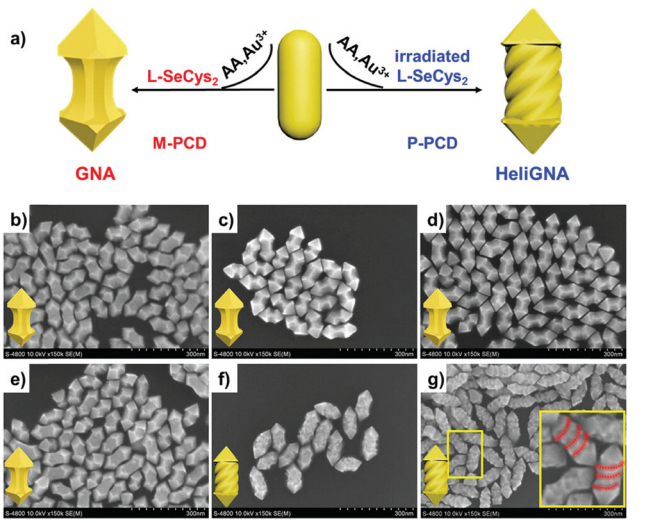

Fig. 4 (a) Schematic illustration of the seed-mediated synthesis of GNAs and HeliGNAs under varying concentrations of L-$SeCys_2$. (b)–(d) SEM images of GNAs synthesized with L-$SeCys_2$ concentrations of 2×10^{-6} M, 6×10^{-6} M and 10×10^{-6} M, respectively. (e)–(g) SEM images of HeliGNAs prepared using irradiated L-$SeCys_2$ (irr-L-$SeCys_2$) at corresponding concentrations of 2×10^{-6} M, 6×10^{-6} M and 10×10^{-6} M. Adapted with permission from ref. 43. Copyright 2021, John Wiley and Sons.

morphologies. In this strategy, a template ranging from biomolecular frameworks such as DNA and peptides to supramolecular or inorganic helices directs the orderly assembly of precursor species *via* physical adsorption and chemical coordination. After growth, the template can be retained or selectively removed to yield a freestanding chiral structure. This approach enables precise control of handedness, periodicity and optical anisotropy across multiple length scales.[46]

Various templating systems have been established to construct chiral nanostructures. DNA origami frameworks, for instance, direct gold nanoparticles into single or double helices that exhibit distinct CD responses arising from collective plasmonic coupling.[47,48] Peptide fibrils such as human islet amyloid polypeptides (hIAPPs) serve as dynamic biotemplates capable of guiding nanorod assembly and amplifying the g-factor of plasmonic bands.[49] More recently, supramolecular assemblies have emerged as highly adaptive chiral scaffolds with tunable handedness and reversible configurational control, enabling efficient chiral information transfer to plasmonic or semiconductor components. For example, co-assembly of L-/D-arginine with porphyrin derivatives (H_2TPPS) generates double-helical frameworks that guide Pt–Au nanorod growth, yielding distinct visible-range CD signals indicative of successful chirality transfer.[50]

Mechanistic origins of chirality. In template-assisted systems, chirality arises through the transcription of a pre-existing chiral morphology or molecular arrangement from the template to the resulting inorganic framework. This process typically proceeds *via* two interconnected mechanisms: (i) the guided organization of building blocks along a chiral host and (ii) the subsequent structural replication of its helical architecture. In the first mechanism, precursor species either pre-synthesized nanoparticles or molecular building units assemble or nucleate directly on the chiral template surface, following its spatially twisted configuration. The chiral host may originate from self-assembled organic systems, such as helical liquid crystals or lipid nanotubes, where molecular dopants or chiral headgroups impose helical ordering on the host matrix. For instance, a nematic liquid crystal doped with S-/R-811 induces a helical supramolecular phase that directs the co-assembly of achiral QDs into helically ordered composites,[51] while lipid nanotubes bearing helically distributed aminophenyl-β-D-glucopyranoside groups template the growth of chiral CdS nanoparticle arrays.[52]

The second mechanism involves organizing inorganic precursors within a chiral matrix followed by removal of the template to yield a stable inorganic structure that preserves the original handedness. A representative example is the use of cellulose nanocrystals (CNCs), which spontaneously form chiral nematic phases that guide the co-assembly of metal oxide precursors into helicoidal TiO_2/Cu_xO architectures. Upon calcination, the organic CNC template is eliminated, yet the chiral nematic morphology remains, confirming the successful transcription of chirality.[53] Similarly, the polycondensation of silane precursors on gemini surfactant assemblies containing L-/R-tartrate counterions generates SiO_2 nanoribbons with

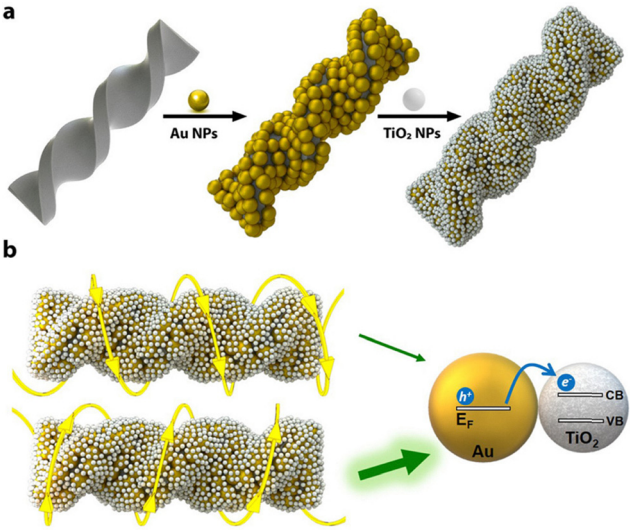

Fig. 5 (a) Schematic illustration of the adsorption of Au and TiO_2 nanoparticles onto chiral SiO_2 nanoribbons. (b) Illustration of the asymmetric interaction between a left-handed (L) hybrid structure and left- or right-circularly polarized (LCP/RCP) light. When the helicity of the nanoparticle assembly matches that of the incident CPL, the hot-electron transfer between the metal Fermi level and the semiconductor conduction band is maximized, enhancing charge separation and photocatalytic efficiency. Adapted with permission from ref. 54. Copyright 2022, American Chemical Society.

opposite handedness. When Au nanoparticles are anchored onto the aminated SiO_2 framework, the resulting SiO_2@Au hybrids exhibit mirror-symmetric CD signals, demonstrating the efficient transfer of chiral information from the template to the plasmonic component through interparticle coupling (Fig. 5).[54]

Overall, chiral templates mediate chirality transfer through a combination of non-covalent and coordination interactions, including hydrogen bonding, van der Waals forces, π–π stacking and electrostatic interactions.[46] These cooperative interactions not only stabilize the templated structure during synthesis but also influence the optical and catalytic properties of the resulting materials. The challenges, however, persist in retaining chiral fidelity after template removal, as excessive interaction strength may cause template residue or structural collapse. Addressing these limitations requires rational template design and a deeper understanding of interfacial chirality transfer mechanisms to achieve scalable synthesis with uniform chiral expression.

Amplification of surface area. The templating strategy not only governs chirality transfer at the molecular and interfacial levels but also profoundly influences the resulting material architecture. The translation of chiral morphology from the template into the inorganic matrix often yields helical or twisted frameworks with structural characteristics that extend beyond optical activity. Among these, the amplification of surface area stands out as a key structural advantage. The intrinsic curvature and periodic helicity of chiral architectures promote the formation of porous, high-surface-area frameworks that facilitate efficient molecular transport and catalytic turnover.

This morphological amplification thus bridges the mechanistic origins of chirality with its functional implications in catalysis, adsorption and light–matter interactions.

The helical morphology inherent to chiral nanostructures confers a substantial increase in accessible surface area, a critical determinant of catalytic efficiency. Unlike planar or lamellar configurations, helical geometries provide a continuous, multidimensional surface that ensures greater exposure of active sites and facilitates mass diffusion across the interface. For instance, helical rod-structured carbon nitride (HRCN) exhibits a surface area nearly 14 times higher than that of bulk carbon nitride, attributed to its coiled configuration and hierarchical porosity encompassing micro-, meso- and macroporous domains.[55] This hierarchical texturing not only maximizes the density of catalytically active sites but also enhances reactant accessibility and charge transport, thereby accelerating surface redox kinetics. The enlarged surface area, when coupled with chiral electronic or optical features, further amplifies reaction pathways and selective responses under polarized illumination. Mathematically, the surface area of a helix is governed by its pitch (p) and radius (r), where smaller pitch and larger radius synergistically enhance curvature and accessible surface exposure, reinforcing the interplay between geometry and function in chiral materials:

$$\text{Surface area} = 2\pi r\sqrt{r^2 + \left(\frac{p}{2\pi}\right)^2}$$

Charge transport optimization. Beyond morphological advantages, particularly the helical arrangement of nanostructures also imparts unique electronic properties that facilitate directional charge migration and minimize recombination losses. Wang *et al.* demonstrated that HRCN exhibits not only superior surface area but also markedly enhanced photogenerated charge separation compared to its achiral counterpart.[55] Similarly, helical nanofilaments demonstrate a 10-fold improvement in charge generation compared to lamellar structures, attributed to optimized light absorption and charge transport facilitated by their geometry.[56] The continuous helical geometry supports coherent charge transport pathways while simultaneously enhancing photon absorption through multiple scattering within the twisted framework. This coupling between structure and function establishes chiral helices as efficient light-harvesting scaffolds capable of synergistically enhancing both optical and electronic responses.

Elucidation of chirality characteristic

Despite the rising number of studies demonstrating the growing potential of chiral nanomaterials, their application in sustainable and green chemical transformations remains relatively underexplored. This limitation largely arises from the complexity of catalytic processes and the challenges in directly correlating molecular chirality with macroscopic catalytic performance. Thus, the elucidation and quantitative assessment of chirality in photo(electro)catalytic systems are critical for understanding how chiral asymmetry governs charge dynamics, spin polarization and interfacial reaction mechanisms. Several advanced characterization techniques have been developed to probe these chiral-specific properties, each offering unique insights into the electronic, optical and spin-dependent phenomena that underlie chiral functionality.

Time-resolved microwave conductivity (TRMC)

One notable method for observing the changes in chiral-induced materials is time-resolved microwave conductivity (TRMC), particularly effective in assessing alterations in electrical characteristics, notably the mobility of charge carriers. Generally, chiral materials exhibit a higher degree of periodic regularity compared to their achiral counterparts. The increased regularity influences the mobility of charge carriers within the material.[57] By employing TRMC, the lifetime of charge carriers within a material can be measured. The TRMC signal is interpreted through the Q value, representing the microwave power loss in the cavity, defined as:

$$Q = \frac{f_0}{\Delta f_0}$$

where f_0 is the resonant frequency and Δf_0 is the full width at half maximum (FWHM) of the Q curve. The relationship between reflected microwave power and conductivity is given by:

$$\langle \Delta\sigma \rangle = \frac{1}{A} \frac{\Delta P_r}{P_r}$$

where $\langle \Delta\sigma \rangle$ is the mean conductivity, A is the sensitivity factor, and $\Delta P_r/P_r$ is the fractional change in reflected microwave power. The change in conductivity, resulting from transient charge carriers with concentration N, is:

$$\Delta\sigma = e \cdot \sum \mu \cdot N$$

where e is the elementary charge and $\sum \mu$ is the sum of charge carrier mobilities. Conductivity depends on the charge carrier concentration, which is influenced by laser-induced carrier generation, as described by Beer–Lambert's law. The photon density at penetration depth Z is:

$$I_{(Z)} = \alpha \ln 10 \times 10^{-\alpha Z} \cdot \phi \cdot I_0$$

where $I_{(Z)}$, I_0, α, and ϕ represent the photon density at position Z, the initial incident photon density minus reflected density, the linear absorption coefficient, and the quantum yield of charge separation per photon, respectively. Therefore, the mean conductivity is:

$$\langle \Delta\sigma \rangle = e \cdot \sum \mu \cdot \varphi \cdot I_0 \cdot F_{\text{Light}}$$

where F_{Light} is the correction factor (or filling factor). This provides a comprehensive framework for analyzing the TRMC signal in terms of charge carrier dynamics.[58–60]

$$\varphi \cdot \sum \mu = \frac{1}{e \cdot A \cdot I_0 \cdot F_{\text{Light}}} \cdot \frac{\Delta P_r}{P_r}$$

Ghosh and colleagues demonstrated chiral (R)-NDI exhibits a significantly enhanced conductivity, with a maximum conductivity $(\varphi \sum \mu)_{\max}$ of 1.7×10^{-5} cm^2 V^{-1} S^{-1} alongside a

long carrier lifetime.[57] Here, ϕ represents photocarrier generation efficiency, and $\Sigma\mu$ denotes the sum of hole and electron mobilities. The TRMC profile of (S)-NDI was also documented similarly, revealing a $(\varphi \sum \mu)_{max}$ of 1.4×10^{-5} cm^2 V^{-1} S^{-1}, which was nearly equivalent to the value observed for (R)-NDI.

Circular dichroism (CD)

CD represents the primary and straightforward method for optically discerning chiral materials with distinct orientations. By subjecting a material to circularly polarized light, CD enables the confirmation of its chirality through differential absorption. Moreover, the direction of chirality becomes apparent as the observed CD signal exhibits positive or negative values depending on the orientation. Furthermore, CD facilitates quantitative evaluation of chirality by determining the dissymmetry factor or *g*-factor associated with the material.[23] When CPL passes through chiral materials, the transmitted light intensity becomes unbalanced due to differential absorption of the CPL components. This phenomenon can be expressed as;

$$\Delta A = A_L - A_R = (\varepsilon_L - \varepsilon_R)CL$$

where A is the absorbance, ε is the molar extinction coefficient, C is the concentration, and L is the path length of the light. CD spectra are characterized by bisignate regions with closely spaced negative and positive peaks, whose sign changes near an extinction band. This behavior is explained by the Cotton effect, resulting from energy level splitting in chiral materials.[61] Due to the polarization-dependent nature of light absorption, the amplitude and spectral position of the CD signal are directly related to electronic transitions from the ground state to the excited state. The rotational strength (R_{0a}) indicates that the absorption of circularly polarized photons is driven by the interaction between the electric dipole transition moment and the magnetic dipole transition moment, as given by;

$$R_{0a} = \mathrm{Im}\left[\langle \Psi_0 | \hat{E} | \Psi_a \rangle \cdot \langle \Psi_a | \hat{M} | \Psi_0 \rangle\right] = \mathrm{Im}\left[\overrightarrow{\mu_{0a}} \cdot \overrightarrow{m_{a0}}\right]$$

where Ψ_0 and Ψ_a are the wave functions for the ground state (0) and excited state (a), $\hat{E}$ and $\hat{M}$ are the electric and magnetic moment operators, and $\overrightarrow{\mu_{0a}}$ and $\overrightarrow{m_{a0}}$ are transient electric and magnetic dipole moments, respectively.[62]

While conventional CD probes intrinsic structural chirality in the absence of external perturbations, magnetic CD (MCD) introduces an additional degree of freedom by breaking time-reversal symmetry through an applied magnetic field. In MCD, differential absorption of circularly polarized light arises from Zeeman splitting of electronic states, enabling direct interrogation of spin-dependent electronic transitions that are inaccessible to natural CD alone.[63,64] Recent studies have demonstrated that chiral materials incorporating paramagnetic centers or open-shell electronic configurations can exhibit pronounced MCD responses, with the chiroptical signal being modulated or even reversed under moderate magnetic fields.[65,66] For example, chiral organic radical ferroelectrics based on charge-transfer complexes have been shown to display coexisting natural CD and MCD signals within the same absorption bands, allowing disentanglement of chirality-induced and magnetically induced optical activity. These observations establish MCD as a powerful probe for correlating chirality, spin polarization and electronic structure, particularly relevant for chiral materials in which spin-selective processes are operative.[66] Extending chiroptical spectroscopy to lower photon energies, terahertz CD (TCD) has emerged as a complementary technique for probing chirality-associated dynamics at mesoscopic length scales and low-energy excitation regimes. Operating in the terahertz frequency range, TCD is particularly sensitive to collective lattice vibrations, soft phonon modes, low-frequency molecular motions and mesoscale helical architectures, providing access to chiral responses that are not captured by electronic CD or MCD.[67,68]

Magnetic conducting atomic force microscopy (mc-AFM)

Magnetic conducting atomic force microscopy (mc-AFM) serves as another valuable technique for confirming the directionality of chirality in chiral materials.[69–71] In mc-AFM measurements, the current flowing between a ferromagnetic AFM tip and the chiral surface is recorded while varying the magnetic field direction.[71] In detail, the spin of the ejected electrons from the perpendicularly magnetized substrate to the deposited chiral material varies depending on the direction of the external magnetic field. The electric potential was applied with the AFM tip set to ground, while the potential on the magnetized substrate was varied. Thus, the spin-selective electron transport was easily measured and quantified by determining the relative ratio of currents with the two different magnet configurations (up and down), expressed as:[72]

$$\text{Spin polarization (SP)} = \frac{(I_{up} - I_{down})}{(I_{up} + I_{down})}$$

The experimental setup is illustrated in Fig. 6a. The corresponding current–voltage (*I–V*) curves, depicted in Fig. 6b and c, were obtained using mc-AFM. Notably, for Au(S)–BT_2T_4, the highest current was observed under the 'Magnet Down' orientation, while the reverse holds for Au(R)–BT_2T_4. The quantitative analysis performed using mc-AFM enables the determination of maximum spin-polarization, which ranges between 28 and 30% under a ±2 V bias, with each value corresponding to a different state of spin polarization.

Low energy photoelectron transmission (LEPET)

Among the techniques employed to verify chirality, one pivotal method used during the discovery of the CISS effect is low energy photoelectron transmission (LEPET) spectroscopy.[73] Göhler demonstrated spin-selective electron transmission through self-assembled monolayers of double-stranded DNA on an Au substrate.[74] The study employed two photoelectron detection methods which are an electron time-of-flight instrument to measure electron kinetic energy distribution and a Mott-type electron polarimeter for spin analysis, using linearly

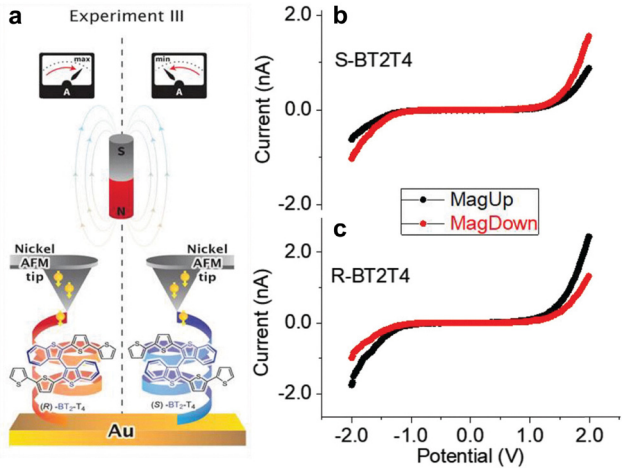

Fig. 6 (a) Schematic illustration of magnetic conductive probe atomic force microscopy (mc-AFM). (b) and (c) *I*–*V* curves obtained by mc-AFM. Adapted with permission from ref. 71, Copyright 2024, John Wiley and Sons.

or circularly polarized light. An electrostatic 90° bender, followed by transport optics, redirected the photoelectrons for direct polarization measurements, converting longitudinal spin polarization into a transverse orientation. In electron polarimeter, the spin polarization of electrons induced a scattering asymmetry described by:

$$A = \frac{(I_{\text{upper}} - I_{\text{lower}})}{(I_{\text{upper}} + I_{\text{lower}})}$$

where I_{upper} and I_{lower} are the count rates in the Mott polarimeter's upper and lower counters. The analyzing power, S_{eff}, also known as the Sherman function, quantifies this spin–orbit interaction. The transverse polarization P is given by:

$$A = P \cdot S_{\text{eff}}$$

The quantum efficiency and kinetic energy distribution of the photoelectrons were recorded based on the relative polarization of light and the chirality of the molecules.[75]

Electron microscopy

Nanoparticles with intrinsic chirality, arising from reduced symmetry and pronounced optical activity, require structural characterization that extends beyond qualitative imaging. Electron microscopy provides a powerful platform for resolving chiral features at the nanoscale, owing to the strong interaction of high-energy electrons with matter and the high spatial resolution that can be achieved. In electron diffraction, crystallographic chirality can be inferred from intensity asymmetries between Bijvoet pairs arising from multiple-beam scattering effects.[76] While effective for well-ordered crystals, conventional electron diffraction yields structural information averaged over many unit cells and is therefore poorly suited for materials with low crystallinity, defects or domain heterogeneity. Diffraction intensities are also highly sensitive to specimen thickness and dynamical scattering, requiring careful experimental control and data processing.

High-resolution transmission electron microscopy (HRTEM) enables direct visualization of crystal structures at atomic resolution under specific imaging conditions. By comparing HRTEM images acquired along different zone axes, the handedness of small zeolite crystals has been successfully determined.[77,78] A range of related electron-based approaches including lattice-fringe analysis in TEM images,[79] electron backscatter diffraction,[80] electron vortex beams,[81] convergent beam electron diffraction[82] and precession electron diffraction[77] have also been explored for handedness determination. However, these methods are generally limited to specific material systems or do not allow definite determination of local handedness at the atomic scale. To access local crystallographic information in complex or twisted structures, current strategies often rely on selected area electron diffraction (SAED), in which different regions of a crystal are aligned to the electron beam *via* goniometer tilting and the angular deviation between zone axes is quantified.[83,84] Complementary methods include crystal orientation mapping based on precession-assisted diffraction spot recognition[85] and nanobeam electron diffraction for resolving local variations in zone-axis orientation.[86] While these approaches improve spatial resolution relative to conventional diffraction, they remain indirect and sensitive to experimental alignment.

In this context, scanning transmission electron microscopy (STEM) has emerged as a particularly powerful technique for atomic-scale chirality analysis. With the introduction of aberration correction, STEM routinely achieves sub-angstrom spatial resolution,[87] enabling robust imaging of chiral structures in weakly crystalline, defective or mixed-enantiomorph materials. Using aberration-corrected STEM, Dong and colleagues developed an electron crystallographic methodology for local determination of crystal handedness at the atomic level. In this approach, pairs of STEM images are acquired from the same crystal by tilting clockwise and anticlockwise between selected zone axes. Comparison of the resulting enantiomorphic projections reveals mirror-related atomic arrangements that directly encode handedness. This method was validated through simulated STEM tilt series and successfully applied to chiral tellurium, tantalum silicide and quartz crystals.[88]

More recently, three-dimensional electron diffraction (3D ED) has further expanded the capability of electron diffraction for chiral materials. By integrating continuous-rotation data acquisition with dynamical diffraction refinement and automated high-throughput analysis, 3D ED enables reliable determination of crystal handedness at the level of individual nanocrystals. Importantly, it also allows statistical quantification of enantiomorphic excess in crystalline powders by analysing large populations of sub-micrometre crystals. As demonstrated in recent work, this approach has been successfully applied to both inorganic chiral nanocrystals and organic molecular crystals, enabling direct correlation between crystal handedness, ligand-directed growth bias and crystallization pathways.[89] Such capability is particularly relevant for chiral nanomaterials

synthesized under kinetically controlled conditions, where ensemble-averaged diffraction techniques fail to resolve local or population-level chirality.

Chemical titration with UV-vis spectroscopy

The spin-selective nature of chiral catalysts, governed by the CISS effect can be experimentally validated through chemical titration coupled with UV-vis spectroscopy. This method provides a quantitative means to probe spin-dependent reaction pathways in photo(electro)catalytic water oxidation. Specifically, it enables indirect observation of spin-controlled radical formation and reaction selectivity by monitoring reactive oxygen intermediates such as *OH and H_2O_2. In water-splitting systems, the CISS effect facilitates spin-aligned electron transfer, promoting parallel spin orientation among adsorbed *OH radicals. This alignment favors the production of triplet oxygen ($^3O_2$) while suppressing undesirable singlet pathways leading to H_2O_2. Conversely, in achiral systems lacking spin filtering, unaligned spins of *OH radicals increase the likelihood of H_2O_2 formation, reflecting inefficient spin injection at the catalyst–electrolyte interface.

Im *et al.* demonstrated that when the spin-dependent current in CoO_x-based photoanodes was aligned with the spin state of surface *OH radicals, H_2O_2 production was significantly suppressed due to the Pauli exclusion principle, which prevents recombination of radicals with identical spin states.[90] Quantitative titration with *o*-tolidine as a redox indicator revealed an absorbance peak at 436 nm corresponding to H_2O_2. The achiral $CoO_x/BiVO_4$ photoanode exhibited a 3.5-fold stronger peak intensity than its chiral $CoO_x/BiVO_4$ counterpart, confirming spin-selective suppression of side reactions. Similarly, Zhang *et al.* reported enhanced spin alignment in chiral Fe_3O_4 nanoparticles, where markedly lower absorbance at 436 nm indicated reduced H_2O_2 formation relative to the achiral analogue.[32]

Multiclass chiral photocatalyst for hydrogen production

The incorporation of chirality into photocatalytic architectures has matured from conceptual novelty to a purposeful strategy for controlling light harvesting, charge dynamics and interfacial reaction pathways. Across plasmonic, polymeric/graphitic, inorganic and hybrid platforms, chirality operates on two complementary fronts: (i) it sculpts the electromagnetic environment (enhancing chiroptical fields, hot-carrier asymmetry and photon absorption) and (ii) it imposes an asymmetric electronic landscape (favoring directional and spin-selective charge transport). Together, these effects can dramatically improve reaction rates and selectivity, often far beyond what geometry or composition alone would predict. The studies summarized below exemplify the diverse material platforms and mechanistic routes through which chirality confers functional advantage, while highlighting common design principles relevant to hydrogen production (Fig. 7). Representative

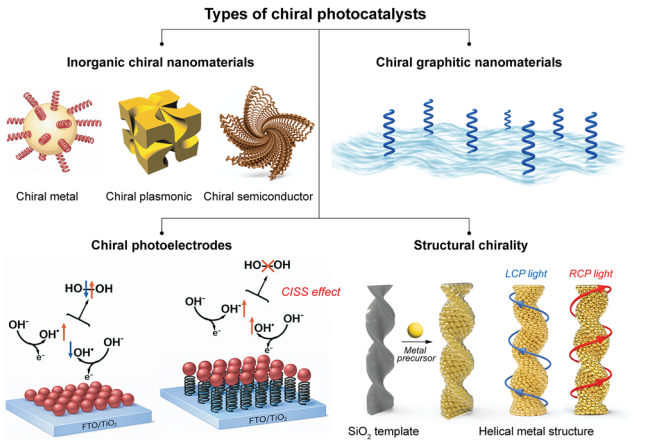

Fig. 7 Schematic overview of representative classes of chiral catalysts employed in photo(electro)catalysis. The figure summarizes inorganic chiral nanomaterials, including chiral metals and plasmonic systems, semiconductors, chiral graphitic nanomaterials, chiral photoelectrodes and structurally chiral systems derived from templating or helical reconstruction. Together, these platforms illustrate the diverse material strategies by which chirality is introduced to modulate light–matter interactions, charge transfer and interfacial reaction pathways in photocatalytic processes.

examples of reported chiral photo(electro)catalysts spanning diverse materials and catalytic reactions are summarized in Tables S1 and S2.

Chiral plasmonic

Plasmonic nanostructures represent an ideal platform for investigating chirality-mediated photochemical processes, as localized surface plasmon resonances (LSPRs) enhance electromagnetic confinement and amplify the influence of structural and molecular asymmetries. Several representative systems have demonstrated that coupling geometric helicity with plasmonic–semiconductor interfaces can generate distinct polarization-dependent charge transfer.

In a related approach, nanoporous optoionic films composed of L-phenylalanine-modified Au nanoparticle multilayers exhibited pronounced CPL-dependent photocurrents, with responses under right-handed CPL approximately 2.4 times higher than those under left-handed CPL.[91] Experimental observations and theoretical analyses reveal that this chiroptical asymmetry arises from the polarization-dependent transduction of CPL into directional charge flow across the chiral nanofilms. The process is driven by light-induced electron ejection mediated through in-plane plasmonic coupling within the nanoparticle layers. The enantiopure Phe ligand shell forms a dense interfacial barrier that prolongs electron lifetimes, while photoinduced charge accumulation at the nanofilm interfaces dynamically reorganizes the surrounding ionic environment within the nanoscale channels, thereby sustaining the helicity-sensitive optoelectronic response. Collectively, such systems underscore the capacity of chiral plasmonic frameworks to mediate asymmetric carrier transport and optically driven charge dynamics. Yet, despite such progress, the

direct application of chiral plasmonic architectures toward photocatalytic hydrogen evolution remains comparatively underexplored.

Recent studies, however, have shown growing potential in integrating optical helicity with catalytic functionality. Hierarchically engineered Au@Pd heterostructures, where twisted Pd nanoarrays are epitaxially grown on chiral Au nanorods, exhibited up to a 2.7-fold increase in photocurrent under helicity-matched CPL, together with a distinct CD response ($g \approx 0.01$).[92] The epitaxial coupling preserves the Au plasmonic resonance while introducing catalytically active Pd sites. The observed polarization-dependent photocurrent enhancement reveals that enantioselective coupling between chiral Au@Pd heterostructures and CPL facilitates directional hot-electron generation, which in turn drives the chiral plasmon-enhanced photocatalytic process. A distinct example of a chiral photo(electro)catalyst for the hydrogen evolution reaction was recently demonstrated by Liu *et al.* in which amino acid–induced branched AgAuPt nanoparticles exhibited pronounced CD spectra and significantly reduced overpotential for hydrogen evolution under CPL compared to unpolarized illumination (Fig. 8).[93] The enhanced activity was attributed to anisotropic plasmonic structures that generated a higher flux of hot electrons under helicity-matched CPL, which synergistically coupled with externally driven charge carriers to accelerate the photoelectrocatalytic process. These findings reinforce that, although chiral plasmonic photocatalysts for hydrogen evolution are still at an early stage, their ability to couple optical helicity with interfacial charge transport offers a promising pathway toward polarization-sensitive and spin-active hydrogen generation.

Chiral carbon nitride

Polymeric graphitic carbon nitride (g-C_3N_4) has become a widely studied metal-free photocatalyst for visible-light-driven hydrogen evolution owing to its suitable band structure, chemical robustness, earth-abundant composition and synthetic simplicity. Since the seminal demonstration of photocatalytic H_2 evolution over g-C_3N_4 in 2009,[94] extensive research efforts have established carbon nitride as a benchmark polymeric semiconductor for photocatalytic HER, as summarized in several comprehensive reviews.[95–100] To address the intrinsic limitations of pristine g-C_3N_4 including rapid charge-carrier recombination, limited visible-light absorption and low electrical conductivity, a wide range of modification strategies has been developed. These include structural engineering (nanosheets, porosity, crystallinity and defect control), elemental doping and construction of heterojunctions or composite architectures to enhance charge separation and interfacial charge transfer. Collectively, these approaches have substantially improved catalytic activity and clarified key structure–property relationships in carbon nitride systems.[98,99,101,102]

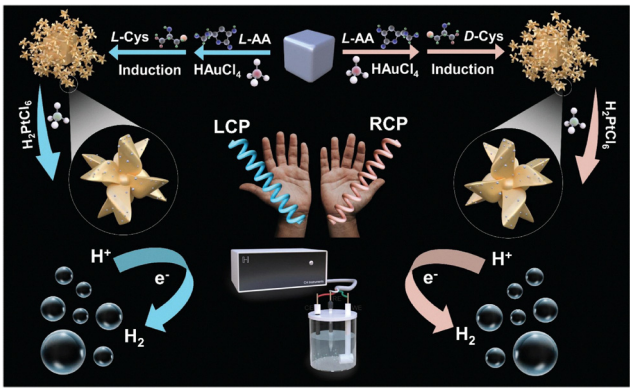

Fig. 8 Schematic illustration of the synthesis of chiral branched AgAuPt nanoparticles and their enantioselective photoelectrocatalytic water-splitting behavior under circularly polarized light (CPL) irradiation. Distinct photocatalytic responses are observed under left- and right-handed CPL, highlighting the chiral-dependent charge transfer dynamics and spin-selective reaction pathways. Adapted with permission from ref. 93. Copyright 2024, Elsevier.

Against this backdrop of well-established electronic and structural optimization strategies, introducing chirality into carbon nitride offers a distinct and less explored pathway to modulate light–matter interactions and charge dynamics beyond conventional band-engineering approaches. Graphitic carbon nitride is attractive for chirality integration because it is abundant, visible-light active and synthetically versatile. When chirality is imposed on its mesoscale morphology, both photonic and electronic properties can be tuned synergistically. Yun *et al.* reported helical-rod g-C_3N_4 (HR-CN) with a sevenfold increase in H_2 evolution (3.7 mmol g^{-1} h^{-1} *vs.* 0.5 for bulk g-C_3N_4). The helical morphology reduces recombination through directional charge transport and improves conductivity along the helix axis, effectively rendering the photocatalyst a one-dimensional charge funnel.[55] Similarly, Lin *et al.* designed mesoporous chiral g-C_3N_4 (MCCN) with integrated photonic effects, observing dramatic gains of H_2 evolution up to 11 mmol g^{-1} h^{-1} ($\approx 55\times$ bulk) and a clear CPL sensitivity (R-CPL produced $\sim 3\times$ greater H_2 than L-CPL). These observations emphasize that chirality at the mesoscale not only increase surface area and light capture but can also couple selectively to polarized light to modulate charge separation and catalytic kinetics.[103]

At the molecular scale, chirality offers an effective means to modulate interfacial charge dynamics in g-C_3N_4-based systems. A supramolecular Pd(II) nanofiber, self-assembled from chiral L-Py ligands, was employed to functionalize g-C_3N_4, yielding L-Py-Pd/g-C_3N_4 with markedly enhanced photocatalytic performance.[104] The chiral catalyst exhibited a hydrogen evolution rate of 2.476 mmol g^{-1} h^{-1}, 85% higher than its achiral racemic analogue (1.339 mmol g^{-1} h^{-1}) and over 80-fold greater than pristine g-C_3N_4 (0.0305 mmol g^{-1} h^{-1}). The enhancement is attributed to the dual functionality of the chiral Pd(II) nanofiber, which operates as both an electron-spin filter and a hydrogen-reduction center. This configuration facilitates spin-selective electron transfer across the g-C_3N_4 interface while suppressing electron–hole recombination, thereby improving carrier utilization under illumination.

Chiral inorganic and hybrid semiconductors

Transferring chirality into rigid inorganic frameworks or composites offers routes to combine structural asymmetry with

defect and dopant engineering. Getaneh *et al.* developed mesoporous TiO_2 structures with a replicated chiral nematic architecture (CNS) using D-glucose as a chiral template. The resulting film displayed ordered cylindrical pores that enhanced light scattering and photocarrier density and further loading with Au nanoparticles as electron collectors produced a fourfold photonic efficiency improvement and an H_2 rate of 11.0 mmol g^{-1} h^{-1} (*vs.* 1.35 for Au-meso-TiO_2). The enhancement stems from the template optical management and the metal role in hot-carrier extraction.[105] Wang and colleagues created asymmetric black TiO_2–SiO_2 microstructures whose helical arrangement promoted oxygen vacancies and Ti–N bonds, extending visible absorption and improving H_2 evolution ($\approx$ 5.0 mmol g^{-1} h^{-1} under sunlight) relative to achiral analogues.[106] Subsequent addition of atomically dispersed Pt increased rates dramatically (to 26.1 mmol g^{-1} h^{-1}), demonstrating that chirality can cooperate with vacancy engineering and single-atom cocatalysts to unlock high activity *via* improved light harvesting and charge separation.[107]

In semiconductor nanorods and frameworks, chirality-ligand interplay is similarly distinct. Ma *et al.* showed that CdSe@CdS nanorods functionalized with cysteine/histidine display length- and diameter-dependent CD signatures and further decoration with multi-site Pt nanocrystals amplified the CD intensity and yielded exceptional H_2 production (75.5 mmol g^{-1} h^{-1} under linearly polarized light). This enhancement can be attributed to the metal-enhanced hybridization of electronic states between the chiral ligand and the achiral nanorods, thus revealing a further improvement in the photocatalytic activities. They also postulated that the interplay between chirality and electron spin transfer, mediated by chiral molecules caused the origin of the substantially improved efficiency observed in the H_2 evolution process.[108] Qian *et al.* constructed Cd-centred MOFs with helical chains templated by pyridyl-leucine derivatives, finding that specific anion coordination (*e.g.*, Cl^- *vs.* formate) modulates recombination and photocurrent where Cd-L_{Cl} exhibited superior photocurrent and H_2 activity due to reduced electron–hole recombination.[109] Meanwhile, Weng *et al.* embedded atomically dispersed Cu(II) in a chiral TpPa(Δ)-COF, with L-cysteine as sacrificial electron donors (SEDs), the resulting chiral COF produced 14.72 mmol g^{-1} h^{-1} H_2, four times the achiral analogue (3.64 mmol g^{-1} h^{-1}), attributable to facilitated cysteine oxidation and enantioselective proton reduction within the stacked chiral framework. The excellent performance can be attributed to the enhanced reaction kinetics for cysteine oxidation and proton reduction kinetics facilitated by the chiral TpPa(Δ)-COF. The chiral 2D COF structure provided a favourable environment for strong enantiomeric interactions with SEDs while enabling parallel stacking of layers, thus effectively reducing energy barriers associated with H_2 production.[110]

Chirality-induced spin selectivity effect (CISS)

Perhaps the most conceptually transformative insight from chiral photocatalysis is the operational importance of spin. The CISS effect, first elucidated by Professor R. Naaman and co-workers, imparts chiral materials with intrinsic spin-filtering capability. As electrons propagate through a helical potential, one spin orientation is preferentially transmitted, resulting in spin-polarized charge transport that modulates interfacial redox kinetics and spin-dependent reaction pathways.[73–75,111] The CISS effect has since been documented across a wide range of energy conversion systems, demonstrating that chirality is not merely a structural descriptor but a functional parameter governing spin dynamics and reactivity.[32,33,112–120] At the experimental level, chiral organic molecules adsorbed on surfaces have been shown to function as electron spin filters at room temperature.[75] When an electron traverses a chiral molecule or material, the helical electrostatic potential can give rise to a curved trajectory that is often described as being analogous to a Lorentz force. In this commonly used picture, an effective magnetic field is generated along the molecular axis, which favors one spin orientation over the other depending on the molecular handedness and transport direction. As a consequence, electron transmission becomes spin dependent, with one spin channel preferentially transmitted, leading to net spin polarization. In this way, molecular chirality defines a preferred spin axis that couples charge transport and spin alignment, thereby influencing electron transfer kinetics at catalytic interfaces.[121] The seminal work by Naaman group reported the first direct evidence of spin-dependent hydrogen evolution on CdSe/TiO_2/FTO photoanodes coated with chiral oligopeptides (Fig. 9).

Compared with achiral analogues, the chiral electrodes exhibited a pronounced decrease in the overpotential required for H_2 generation. Strikingly, under low bias ($\eta < 0.5$ V *vs.* Ag/AgCl), H_2 evolution occurred exclusively on the chiral electrodes, whereas the achiral systems required higher potentials to achieve measurable activity. This finding was remarkable, given that the chiral molecules were longer and more resistive, yet produced higher photocatalytic performance. The authors proposed that upon excitation of CdSe, spin-polarized electrons are transferred through the chiral molecular layer, generating holes with matching spin alignment within CdSe. This spin-correlated process lowers the energetic barrier for proton reduction and facilitates efficient H_2 evolution even under milder driving potentials.[33,75]

While spin-filtered electron transport directly enhances hydrogen evolution, the overall efficiency of photocatalytic water splitting ultimately hinges on the oxygen evolution reaction (OER), whose spin-forbidden nature often constitutes the rate-determining bottleneck. In this context, the CISS effect also emerges as a critical means of accelerating the spin-dependent oxidation pathway. Ai *et al.* synthesized chiral ZnO photocatalysts by coordinating Zn^{2+} ions asymmetrically with L-/D-methionine, thereby creating spin-filtering active sites. The chiral ZnO exhibited prolonged carrier lifetimes (2.4-fold and 1.2-fold for L- and D-ZnO, respectively) and enhanced O_2 generation rates of $\sim$1.31 and 1.29 mmol g^{-1} h^{-1}, compared with 0.80 mmol g^{-1} h^{-1} for achiral ZnO. Rotating ring-disk electrode (RRDE) measurements revealed that both L-/D-ZnO facilitated higher electron transfer numbers, indicative of effective

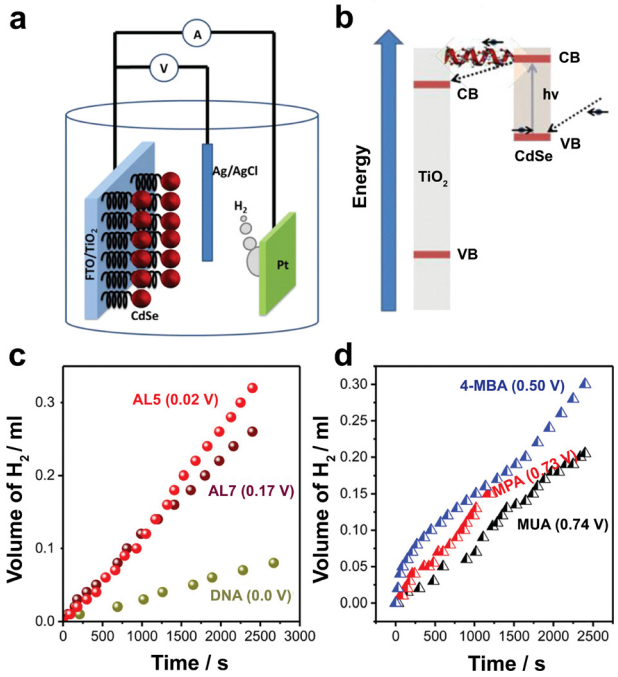

Fig. 9 (a) Scheme of the photoelectrochemical cell used in this study for water splitting. CdSe nanoparticles (red) are bound to TiO_2 nanoparticles through chiral molecules. The TiO_2 nanoparticles are attached to the FTO conducting electrode. On the Pt electrode, H^+ ions are reduced to form H_2. (b) Scheme of electron transfer between S_2^- and TiO_2 nanoparticles. Upon excitation of CdSe nanoparticles, the excited electrons are transferred through the chiral molecules to TiO_2, then to the external circuit. This is a spin-specific electron transfer because the transfer through the chiral molecule is preferred for one spin over the other. Thus, the hole in CdSe has a well-defined spin alignment. Hydrogen production as a function of time for (c) chiral molecules and (d) achiral molecules. The potentials in brackets refer to the overpotential. Adapted with permission from ref. 33. Copyright 2015, American Chemical Society.

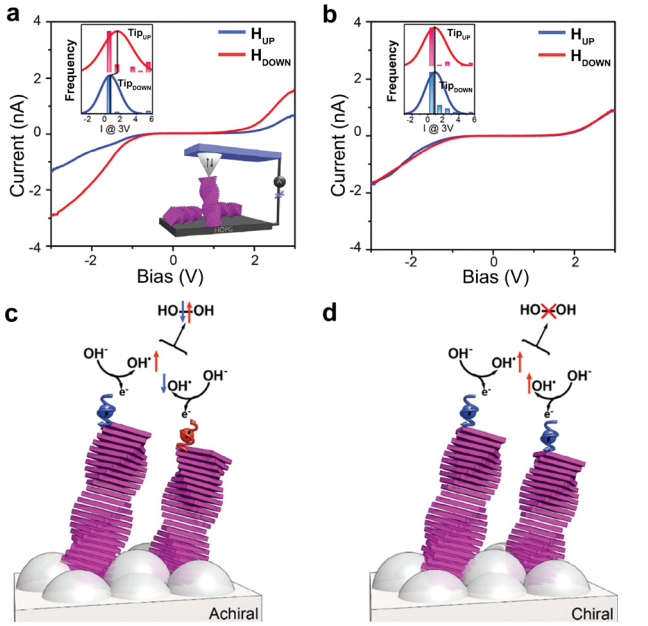

Fig. 10 Magnetic conducting atomic force microscopy (mc-AFM) measurements on stacks of chiral and achiral Zn-porphyrins. The current as a function of the applied voltage for chiral (a) and achiral (b) Zn–porphyrin molecules. Insets show corresponding current histograms at 3 V for two opposite magnetic orientations of the tip. (c) When electron transfer to the anode is non-spin-specific, the spins of the unpaired electrons on the two $OH^\bullet$ are aligned antiparallel, leading to interaction on a singlet surface and the production of hydrogen peroxide (H_2O_2). (d) When electron transfer to the anode is spin-specific, the spins of the two electrons are aligned parallel, causing the two $OH^\bullet$ to interact on a triplet surface, which forbids the formation of H_2O_2 and facilitates the production of oxygen in its ground state. Adapted with permission from ref. 113, Copyright 2017, American Chemical Society.

suppression of the two-electron H_2O_2 pathway. UV-vis titration using *o*-tolidine further confirmed the achiral ZnO showed a strong H_2O_2 peak at 436 nm, while chiral ZnO exhibited a 5.5-fold reduction in signal. Complementary *in situ* EPR analyses further demonstrated that the generation of $^\bullet OH$ radicals was roughly doubled for chiral ZnO, confirming that spin-polarized holes accelerate the triplet O_2 pathway and suppress parasitic peroxide formation. These results collectively highlight how spin-selective charge separation within chiral semiconductors can modulate radical pairing dynamics, thereby enhancing OER selectivity and efficiency.[9]

The spin-selective control of charge transfer was further extended to organic semiconductors by Naaman and co-workers, who examined chiral and achiral aggregates of zinc porphyrins and tri(pyrid-2-yl)amine trisamide (TPyA) (Fig. 10).[113] Their chiral photoanodes exhibited markedly higher photocurrent densities than the racemic counterparts, alongside negligible H_2O_2 accumulation during water oxidation. The suppression of peroxide formation was attributed to the parallel spin alignment of photoexcited electrons, which promotes the coupling of two $^\bullet OH$ radicals on a triplet potential surface, yielding ground-state O_2 instead of singlet H_2O_2. Using mc-AFM, the team confirmed that current directionality in chiral porphyrin stacks depended on the magnetic field orientation, clear evidence of spin preference. In contrast, achiral films exhibited no such dependence, reaffirming that the spin-selective transmission arises intrinsically from molecular helicity.[113] This principle extends beyond molecular semiconductors to layered materials. Bai *et al.* reported similar spin-mediated suppression of H_2O_2 during photoelectrochemical water oxidation on chiral TiS_2 nanosheets,[122] while Im *et al.* achieved notable OER enhancement in chiral CoO_x thin films (Fig. 11).[90] Through liquid-state Raman and FTIR spectroscopy, they elucidated the mechanism of chirality transfer from molecular ligands to inorganic lattices, revealing that the degree of structural distortion dictated the extent of spin filtering. The resulting CoO_x films displayed ~25% higher photocurrent density and ~30% higher O_2 Faradaic efficiency than achiral analogues, owing to selective triplet O_2 generation and the suppression of spin-mismatched intermediates.[90] Most recently, Zhang *et al.* demonstrated that coupling α-Fe_2O_3 with chiral L-cysteine and L-glutathione monolayers significantly improved photoelectrochemical charge transport. The helical electromagnetic fields generated by these monolayers aligned the spins of charge carriers within the hematite layer, reducing charge migration resistance and increasing carrier density by ~61%, accompanied by a fourfold enhancement

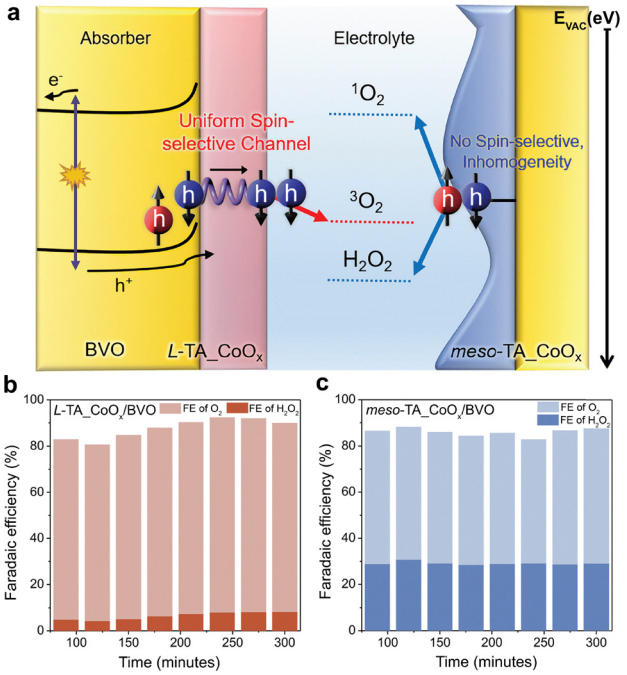

Fig. 11 (a) Schematic illustration of the surface of CISS-based OER devices with chiral L-TA_CoO$_x$/BVO and achiral meso-TA_CoO$_x$/BVO. Calculated faradaic efficiency for O_2 and H_2O_2 shown in a stacked bar chart for (a) L-TA_CoO$_x$/BVO and (b) meso-TA_CoO$_x$/BVO based on photocurrent generation. Adapted with permission from ref. 90. Copyright 2023, The Royal Society of Chemistry.

in photocurrent density compared to achiral interfaces. This observation provides further evidence that interfacial chiral fields can act as spin injectors, tuning charge transfer energetics without altering the bulk semiconductor structure.[123]

Across these classes several convergent lessons appear. First, chirality is not merely a geometrical curiosity. It is a functional handle that modifies electromagnetic fields, local density of states and spin populations in ways that directly influence photo(electro)catalytic pathways. Second, chirality synergizes particularly well with photonic/textural management (*e.g.*, helical porosity) and with atomic-scale engineering (vacancies, single atoms, plasmonic gaps), the combination often yields multiplicative gains. Third, helicity matching between incident CPL and structural handedness can further amplify activity by maximizing hot-carrier asymmetry or selective excitation. Finally, the CISS effect reframes catalyst design with controlling spin is now a viable lever for steering multi-electron, multi-step reactions such as water oxidation and proton reduction. Taken together, these developments position chiral photo(electro)-catalysts as a potent, design-rich frontier for hydrogen production. The field now faces the task of translating these mechanistic insights into robust, scalable architectures and of developing predictive frameworks (theory + *in situ*/*operando* spectroscopy) that link chirality metrics to catalytic metrics. With that roadmap, chirality could evolve from a performance booster in selected systems to a general design principle for next-generation solar-to-chemical technologies.

Beyond hydrogen production

Photocatalytic CO_2 reduction reaction (CO_2RR)

Effective CO_2 activation typically begins with electron transfer into its π^* orbital, forming a $CO_2^{\bullet-}$ or M–COOH intermediate. In this step, spin-polarized electrons play a decisive role by facilitating charge separation, suppressing recombination and steering the spin state of reactive intermediates toward preferred pathways.[124–126] As previously demonstrated, the spin configuration of the M–COOH intermediate critically determines CO_2RR selectivity, where protonation at the oxygen site leads to CO formation, whereas protonation at the carbon site yields formate (HCOOH). The bonding strength between the metal center and COOH, as well as the distribution of electron density are governed by the spin state of the metal where low-spin states tend to favor CO formation, while high-spin configurations stabilize HCOOH production. This mechanistic insight underscores that deliberate modulation of spin populations, whether through ligand field tuning, chirality or spin polarization, can effectively control catalytic selectivity.[127]

From the perspective of chiral photocatalysts, this principle takes on additional significance. As previously discussed, CISS effect provides an intrinsic means of generating spin-polarized charge carriers without relying on external magnetic fields. Recent advances have demonstrated that coupling CISS with light-induced processes can dramatically enhance CO_2 reduction efficiency. For instance, chiral BiOBr/Au hybrid photocatalysts have shown that the combination of plasmonic excitation and CISS synergistically amplifies spin-polarized electron generation. The SPR of Au nanoparticles not only extends the light absorption range but also prolongs carrier lifetime by promoting spin-polarized electron–hole separation. Consequently, the chiral D-BiOBr/Au system exhibited a CO yield more than twice that of its achiral counterpart, confirming that plasmon-mediated spin enhancement offers a viable route to boost photocatalytic CO_2 conversion.[128] Chirality-regulated spin polarization has also been successfully implemented in perovskite-based photocatalysts. Incorporating chiral organic molecules such as (*R*)- or (*S*)-methylbenzylamine bromide (MBA:Br) into all-inorganic $CsPbBr_3$ nanoplates produces chiral Ruddlesden–Popper perovskite (RPP)/nanoplate hybrids that exhibit pronounced chiroptical activity. The resulting spin-polarized carriers significantly suppress charge recombination, enhancing the photocatalytic CO_2 reduction rate (Fig. 12). Under an external magnetic field of 0.3T, the chiral perovskite photocatalysts achieved up to a fivefold increase in CO_2 reduction efficiency compared to pristine $CsPbBr_3$ nanoplates. These findings establish that manipulating spin polarization through structural chirality offers a controllable and synergistic route to enhance charge transport and catalytic performance in perovskite systems.[129]

Beyond perovskites, chirality has been harnessed in semiconductor frameworks to drive complex multi-electron and multi-proton reduction processes. In particular, chiral mesostructured Cu–In_2S_3 photocatalysts demonstrated exceptional selectivity ($\approx$ 93.7%) for ethanol under solar irradiation, driven

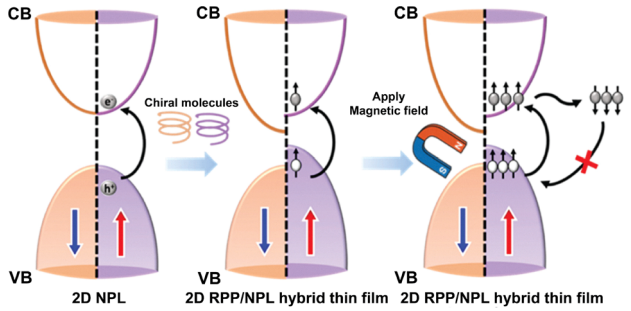

Fig. 12 Schematic illustration of the prolonged photoexcited carrier lifetime in chiral 2D RPP/NPL hybrids induced by electron spin polarization under an external magnetic field. The applied field aligns spin states, suppressing charge recombination and enhancing spin-selective charge transport within the chiral perovskite framework. Adapted with permission from ref. 129. Copyright 2025, American Chemical Society.

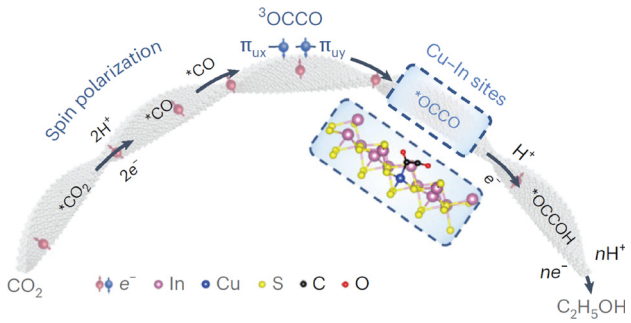

Fig. 13 Schematic illustration showing how reactive Cu–In dual sites facilitate the conversion of spin-polarized intermediates into chemisorbed *OCCO and *OCCOH species. The cooperative interaction between Cu and In centers promotes C–C coupling, thereby accelerating the overall reaction kinetics. Adapted with permission from ref. 7 Copyright 2025, Springer Nature.

by chirality-induced spin polarization that stabilized triplet OCCO intermediates (Fig. 13). The presence of reactive Cu–In dual sites facilitated the conversion of these spin-polarized intermediates into chemisorbed *OCCO and *OCCOH species, accelerating C–C coupling and suppressing undesired C_1 by-products. This work highlights how spin-selective charge transfer mediated by chirality can direct the reaction toward higher-order carbon products, a critical advancement in solar-driven CO_2 reactions.[7] Meanwhile, the introduction of chirality into polyoxometalate-based frameworks has yielded substantial improvements in catalytic performance. Chiral $[Co(C_{12}H_8N_2)(H_2O)]_2[(C_6H_5PO_3)_2Mo_5O_{15}]$ photocatalysts exhibited nearly threefold enhancement in CO generation compared to their achiral analogues, despite possessing comparable structural composition. The formation of helical two-dimensional layers within these chiral frameworks facilitated asymmetric charge distribution and more efficient electron transfer to CO_2 molecules. This finding exemplifies how intrinsic structural chirality, independent of external magnetic or plasmonic effects, can enhance charge transport, stabilize reactive intermediates and substantially elevate photocatalytic CO_2 reduction efficiency.[130]

Recent developments have extended the scope of photocatalytic CO_2 reduction beyond conventional small-molecule products such as CO, CH_4 and CH_3OH, toward the selective synthesis of high-value chemical feedstocks. Recently, chiral ZnS mesostructures have demonstrated the capacity to bridge solar-to-fuel and solar-to-chemical conversion by achieving enantioselective amino acid synthesis directly from CO_2 and NH_3. The oriented helical lattice of chiral mesostructured ZnS (CMZ) induced strong spin polarization, aligning electron spins in parallel and stabilizing triplet *OCCO intermediates. This alignment promoted efficient C–C coupling between C_2 and C_1 species, yielding amino acids such as serine with enantiomeric excess exceeding 96%. The helical distortion of the CMZ lattice further reduced the free energy of *OCCO formation, facilitating spin-selective asymmetric carbon–nitrogen coupling and establishing a pathway for abiotic CO_2 fixation into chiral biomolecules.[131] From a mechanistic standpoint, this study reinforces that chirality functions not merely as a structural or optical descriptor but as an active spin-control element governing charge carrier dynamics and product selectivity. The integration of CISS effects with plasmonic resonance, perovskite lattice engineering and semiconductor heterojunctions provides a versatile platform for tailoring spin-selective charge transfer, thereby expanding the conceptual boundaries of CO_2 photoreduction toward both energy fuels and chiral chemical synthesis.

Photocatalytic N_2 reduction reaction (N_2RR)

Reducing molecular nitrogen (N_2) to ammonia under light irradiation remains exceptionally challenging due to the high dissociation energy of the N≡N bond and the stringent requirement for synchronized proton–electron transfer.[132] Although N_2 is diamagnetic and thus exhibits minimal sensitivity to spin polarization during its initial adsorption, spin effects become crucial at later stages, particularly during the formation and hydrogenation of key intermediates such as *NNH. In biological nitrogenase systems, Fe centers play an essential role in weakening the N≡N bond through electron back-donation and successive protonation steps.[133,134] Low-coordination Fe sites have been shown to promote more effective N≡N activation than their highly coordinated counterparts, owing to their increased orbital flexibility and enhanced capacity for electron redistribution. Furthermore, Fe oxides such as magnetite (Fe_3O_4) possess intrinsic magnetic moments, rendering them particularly relevant for spin-sensitive nitrogen reduction reaction (N_2RR) pathways.[135–137] Meanwhile, Dai *et al.* proposed nitrate (NO_3^-) reduction (NITRR) as an energetically favorable analogue to N_2RR, given its lower bond dissociation energy (204 kJ mol^{-1}) and environmental ubiquity in wastewater and acidified rivers.[138–142] They engineered Fe single atoms anchored on Ti foam, where adjacent oxygen-deficient TiO_2 layers induced synergistic spin polarization across Fe and Ti centers. The resulting unpaired electrons promoted spin-compatible interactions with NO_3^- and its hydrogenated intermediates, facilitating efficient proton–electron coupling during *NO formation and beyond. This spin-cooperative architecture

achieved impressive nitrate reduction activity, yet a full translation to chiral N_2RR or NITRR remains unrealized.

Emerging directions beyond water splitting and small-molecule reduction

Beyond water splitting and small-molecule reduction, emerging studies demonstrate that chirality can be exploited to steer a broader spectrum of light-driven transformations by regulating charge separation, carrier transport and reaction selectivity. In these systems, chirality operates as an active design parameter that couples photonic excitation to reaction pathways, enabling access to catalytic regimes not readily achievable with achiral architectures. A representative example is the handedness-dependent switching between photocatalytic and photothermal pathways reported by Wang and co-workers using Au@CdS nanoparticles functionalized with chiral cysteine ligands.[143] When the handedness of CPL matched the catalyst chirality, spin-polarized charge transfer was promoted, yielding efficient photocatalytic H_2 evolution. In contrast, mismatched helicity favored spin-forbidden recombination and localized heating, redirecting the reaction toward photothermal methanol reforming. This reversible switching behavior illustrates how chirality can dictate reaction pathways under identical illumination conditions, enabling methanol reforming at substantially lower effective temperatures than conventional thermal processes.

Chirality-mediated control has also been extended to photocatalytic environmental remediation, where advanced oxidation processes depend critically on efficient charge utilization. Early studies showed that chiral coordination complexes and chiral semiconductor nanostructures suppress electron–hole recombination and enhance pollutant degradation. For example, chiral metal–salen complexes immobilized on polyoxometalate scaffolds and chiral Ag_xCd_yS-based nanoparticles achieved degradation efficiencies exceeding 90% for Rhodamine B and methylene blue under visible light.[144,145] In the latter system, chiral organization led to nearly an order-of-magnitude increase in photocurrent relative to achiral analogues and enabled enantioselective photoreduction of Cr^{6+} with reaction rates enhanced by ~20% when catalyst and sacrificial molecules shared matched handedness.[145] Titanium-oxide-based platforms further demonstrate how chirality introduces selectivity into remediation reactions. Molecular imprinting of chiral herbicides onto single-crystalline TiO_2 nanorods enabled preferential photoelectrochemical degradation of the environmentally persistent (*S*)-enantiomer of dichlorophenoxypropionic acid, with rates ~2.6-fold higher than those of the opposite enantiomer.[146] Photonic TiO_2 films templated from cellulose nanocrystals similarly exhibited a fourfold increase in charge carrier density and ~1.5-fold enhancement in phenol degradation activity compared with mesoporous TiO_2.[147]

Plasmonic chiral architectures introduce an additional level of control by coupling structural chirality with localized electromagnetic field enhancement. Helical SiO_2@Au@TiO_2 structures and cysteine-functionalized gold–gap–silver nanostructures display pronounced polarization-dependent photocatalytic responses under CPL, in contrast to their achiral counterparts. In these systems, helicity-matched excitation governs hot-carrier generation and transfer, providing mechanistic insight that extends to other chiral photocatalytic processes, including polarization- and spin-selective hydrogen evolution. Collectively, these studies establish chirality as a unifying handle for modulating interfacial kinetics and reaction selectivity across diverse light-driven transformations from methanol reforming to pollutant degradation.

Outlook

Chirality has evolved from a mere structural descriptor into a unifying design principle that governs light–matter and spin–matter interactions at catalytic interfaces. Despite solid conceptual advances, the field remains at a formative stage where mechanistic interpretations are often suggestive rather than conclusive. Realizing the full technological potential of chiral photocatalysis requires an integrative framework that bridges theoretical modeling with operando spectroscopy, surface chemistry and device engineering.

(1) A central and urgent challenge is to establish quantitative correlations between rigorous chirality descriptors (for example, CD spectra, dissymmetry factors g_{abs} or g_{lum}, and spin-polarization percentages) and catalytic performance metrics (turnover frequency, apparent quantum yield, products evolution rate, selectivity and stability).[110] Current reports often present chiroptical or spin-sensitive observables in isolation from catalytic benchmarks, which prevents mechanistic linkage and obscures whether measured asymmetries directly modulate charge separation, intermediate binding energies or key multielectron steps.[148] This decoupling hinders the mechanistic understanding of how CISS effect or optical chirality directly modulates charge separation, surface adsorption or intermediate stabilization.[149] Establishing unified descriptors that link optical asymmetry with catalytic efficiency would be transformative, allowing chirality to be treated as an intrinsic photocatalytic variable rather than a secondary structural feature.

(2) Mechanistically, spin-polarized charge dynamics under photocatalytic conditions remain insufficiently characterized. While the CISS effect has been invoked to rationalize enhanced activity in chiral metal oxides, perovskites and quantum dots, experimental validation is still dominated by indirect observables, including changes in photocurrent response or product selectivity. These measurements, however, offer limited temporal and spin sensitivity and are unable to directly resolve the ultrafast spin-dependent charge-transfer events that underpin CISS-driven catalysis. The integration of operando and spin-resolved spectroscopies such as time-resolved magnetic circular dichroism, spin-resolved photoemission and chiral transient absorption spectroscopy provides a promising pathway to directly interrogate how spin-polarized carriers migrate across interfaces and modulate multi-electron reaction kinetics. Complementary techniques, including terahertz (THz) emission

spectroscopy (TES),[150] spin-polarized scanning tunneling microscopy (SP-STM), electron energy loss spectroscopy (EELS) and nuclear magnetic resonance (NMR), could further elucidate charge delocalization, interfacial coupling and spin–lattice interactions across relevant time and length scales.[151–153] When correlated with isotope labeling, transient absorption and femtosecond pump–probe measurements, these approaches could decisively clarify whether chirality primarily governs initial charge separation or instead regulates subsequent chemical transformation steps.

(3) From a theoretical standpoint, current models remain largely focused on ground-state descriptions, thereby overlooking the spin-dependent excitonic dynamics that shape chiral photochemistry. Advancing time-dependent, spin-polarized DFT and non-collinear molecular dynamics frameworks will be essential to elucidate how chiral potentials influence exciton lifetimes, carrier distribution and reaction barriers.

(4) Material design strategies should prioritize chemically robust and photocatalytically active chiral architectures that preserve their structural and optical characteristics under irradiation. Transitioning from labile molecular templates to covalently integrated systems such as chiral covalent organic frameworks (COFs), helical perovskites, twisted van der Waals heterostructures or chiral plasmonic–semiconductor hybrids will be pivotal. Embedding chiral ligands at semiconductor surfaces could induce spin-polarized energy alignment, enhancing charge separation and suppressing back recombination. Coupling chirality with defect engineering, vacancy modulation or single-atom catalysis could further enable site-specific spin control and selectivity in photocatalytic pathways, particularly for multielectron processes such as CO_2 reduction, nitrate fixation or O_2 evolution.

(5) Beyond material innovation, standardized experimental protocols are needed to ensure reproducibility and comparability. Reporting optical (g_{abs}, g_{lum}), spin (polarization percentage) and photocatalytic (quantum yield, stability, turnover frequency) metrics in parallel, while employing appropriate achiral and racemic controls, will allow systematic evaluation of chiral contributions. Additionally, helicity-swapped illumination or external magnetic perturbations can help disentangle photonic and spin effects, clarifying whether observed enhancements arise from CISS, optical asymmetry or morphology-induced anisotropy.

(6) The integration of chirality into device-level architectures represents the next transformative step. Embedding chiral photocatalysts for instance within photoelectrochemical cells or Z-scheme systems could yield measurable advantage such as reduced overpotentials, improved carrier lifetimes or enhanced selectivity for water splitting reaction, CO_2-to-fuels and NH_3 synthesis. Practical implementation, however, demands scalable and facile fabrication routes, such as chiral templating, self-assembled helical nanofilms or roll-to-roll deposition of chiral metasurfaces. Moreover, parallel assessment of stability, photodegradation resistance and techno-economic viability will be essential for translating chiral photocatalysis from laboratory prototypes to functional solar-driven devices.

Ultimately, the vision extends beyond demonstrating isolated examples of ''chiral enhancement''. The goal is to establish chirality as a predictive and tunable design variable in photocatalysis, one that governs spin, energy and charge flow across the interface. Achieving this vision requires a transition from qualitative observation to quantitative, mechanistic understanding supported by *in situ*/*operando* characterization, advanced computation and integrated device studies. If these challenges are systematically addressed, chirality could redefine the paradigms of light-driven catalysis, enabling precise spin and energy control across multielectron transformations central to sustainable solar fuel generation and energy conversion.

Author contributions

D. H. Kim and Z. Lin supervised the overall project. N. A. R. Che Mohamad drafted the outline and composed the manuscript. D. Won, H. Kang, J. Kim, K. Chae, M. Kim and M. Zhang assisted in conducting a literature analysis. All the authors have reviewed and approved the final manuscript.

Conflicts of interest

There are no conflicts to declare.

Data availability

No primary research results, software or code were included and no new data were generated or analysed as part of this review. The supporting data are included as part of the supplementary information (SI). See DOI: https://doi.org/10.1039/d5ey00314h.

Acknowledgements

This work was supported by Basic Science Research Program (Priority Research Institute) through the National Research Foundation (NRF) of Korea funded by the Ministry of Education (MOE) (2021R1A6A1A10039823) and by the NRF funded by the Korea government (MSIT and MOE) (No. RS-2025-16063688; RS-2025-02982993; RS-2024-00461946). Z. L. acknowledges the financial support from the Ministry of Education (MOE), Singapore, under its Academic Research Fund Tier 2 program (T2EP50224-0011) and (T2EP50125-0010).

References

1 P. Zhang and X. W. (David) Lou, *Adv. Mater.*, 2019, **31**, 1900281.
2 J. He and C. Janáky, *ACS Energy Lett.*, 2020, **5**, 1996–2014.
3 V. Andrei, Q. Wang, T. Uekert, S. Bhattacharjee and E. Reisner, *Acc. Chem. Res.*, 2022, **55**, 3376–3386.
4 J. Hong, C. Xu, B. Deng, Y. Gao, X. Zhu, X. Zhang and Y. Zhang, *Adv. Sci.*, 2022, **9**, 2103926.

5 M. Crespo-Quesada and E. Reisner, *Energy Environ. Sci.*, 2017, **10**, 1116–1127.
6 S. He, Y. Chen, J. Fang, Y. Liu and Z. Lin, *Chem. Soc. Rev.*, 2025, **54**, 2154–2187.
7 Y. Cui, Y. Wang, Y. Ma, X. Su, R. Tai, M. Jia, J. Chen, A. Liu, L. Yu, C. Tian, W. Zhang, L. Han, S. Che and Y. Fang, *Nat. Synth.*, 2026, **5**, 117–128.
8 E. Studer, S. Mandal, T. Stünkel and R. Gilmour, *Angew. Chem., Int. Ed.*, 2025, **64**, e202513320.
9 M. Ai, L. Pan, C. Shi, Z. F. Huang, X. Zhang, W. Mi and J. J. Zou, *Nat. Commun.*, 2023, **14**, 4562.
10 K. Chae, N. A. R. Che Mohamad, J. Kim, D.-I. Won, Z. Lin, J. Kim and D. H. Kim, *Chem. Soc. Rev.*, 2024, **53**, 9029–9058.
11 W. Fu, L. Tan and P. Wang, *ACS Nano*, 2023, **17**, 16326–16347.
12 S. Li, X. Xu, L. Xu, H. Lin, H. Kuang and C. Xu, *Nat. Commun.*, 2024, **15**, 3506.
13 L. Kachtík, D. Citterberg, K. Bukvišová, L. Kejík, F. Ligmajer, M. Kovařík, T. Musálek, M. Krishnappa, T. Šikola and M. Kolíbal, *Nano Lett.*, 2023, **23**, 6010–6017.
14 M. Kim, M. Zhang, Y.-L. Zhu, Y. Yan, X. Pu, W. Choi, S. Chung, K. Cho, J. Kim, V. Tsukruk, Z. Yang, N. A. Kotov, Z.-Y. Lu, D. H. Kim and Z. Lin, *Science*, 2025, **389**, eadu0296.
15 W. Ma, L. Xu, A. F. de Moura, X. Wu, H. Kuang, C. Xu and N. A. Kotov, *Chem. Rev.*, 2017, **117**, 8041–8093.
16 Y. Shao, G. Yang, J. Lin, X. Fan, Y. Guo, W. Zhu, Y. Cai, H. Huang, D. Hu, W. Pang, Y. Liu, Y. Li, J. Cheng and X. Xu, *Theranostics*, 2021, **11**, 9262–9295.
17 A. Döring, E. Ushakova and A. L. Rogach, *Light: Sci. Appl.*, 2022, **11**, 75.
18 S. W. Im, H.-Y. Ahn, R. M. Kim, N. H. Cho, H. Kim, Y.-C. Lim, H.-E. Lee and K. T. Nam, *Adv. Mater.*, 2020, **32**, 1905758.
19 H. Yao, K. Miki, N. Nishida, A. Sasaki and K. Kimura, *J. Am. Chem. Soc.*, 2005, **127**, 15536–15543.
20 H. Yang, J. Yan, Y. Wang, G. Deng, H. Su, X. Zhao, C. Xu, B. K. Teo and N. Zheng, *J. Am. Chem. Soc.*, 2017, **139**, 16113–16116.
21 Y. Zhou, M. Yang, K. Sun, Z. Tang and N. A. Kotov, *J. Am. Chem. Soc.*, 2010, **132**, 6006–6013.
22 S. D. Elliott, M. P. Moloney and Y. K. Gun'ko, *Nano Lett.*, 2008, **8**, 2452–2457.
23 H.-E. Lee, H.-Y. Ahn, J. Mun, Y. Y. Lee, M. Kim, N. H. Cho, K. Chang, W. S. Kim, J. Rho and K. T. Nam, *Nature*, 2018, **556**, 360–365.
24 J. Zheng, C. Boukouvala, G. R. Lewis, Y. Ma, Y. Chen, E. Ringe, L. Shao, Z. Huang and J. Wang, *Nat. Commun.*, 2023, **14**, 3783.
25 L. Tan, Z. Wen, Y. Jin, W. Fu, Q. Gao, C. Xiao, Z. Chen and P. Wang, *Nano Lett.*, 2024, **24**, 13678–13685.
26 Y. Gu, W. Wang, C. Gao, L. Feng, J. Wu and L. Zhao, *CrystEngComm*, 2022, **24**, 4955–4961.
27 Y. Li, J. Cheng, J. Li, X. Zhu, T. He, R. Chen and Z. Tang, *Angew. Chem., Int. Ed.*, 2018, **57**, 10236–10240.
28 Y. Liu, H. Li, S. Li, X. Zhang, J. Xiong, F. Jiang, Y. Liu and P. Jiang, *ACS Appl. Mater. Interfaces*, 2021, **13**, 60933–60944.
29 J. K. Choi, B. E. Haynie, U. Tohgha, L. Pap, K. W. Elliott, B. M. Leonard, S. V. Dzyuba, K. Varga, J. Kubelka and M. Balaz, *ACS Nano*, 2016, **10**, 3809–3815.
30 K. Varga, S. Tannir, B. E. Haynie, B. M. Leonard, S. V. Dzyuba, J. Kubelka and M. Balaz, *ACS Nano*, 2017, **11**, 9846–9853.
31 U. Tohgha, K. K. Deol, A. G. Porter, S. G. Bartko, J. K. Choi, B. M. Leonard, K. Varga, J. Kubelka, G. Muller and M. Balaz, *ACS Nano*, 2013, **7**, 11094–11102.
32 W. Zhang, K. Banerjee-Ghosh, F. Tassinari and R. Naaman, *ACS Energy Lett.*, 2018, **3**, 2308–2313.
33 W. Mtangi, V. Kiran, C. Fontanesi and R. Naaman, *J. Phys. Chem. Lett.*, 2015, **6**, 4916–4922.
34 H. Cao, E. Yang, Y. Kim, Y. Zhao and W. Ma, *Adv. Sci.*, 2024, **11**, 2306979.
35 N. Suzuki, Y. Wang, P. Elvati, Z.-B. Qu, K. Kim, S. Jiang, E. Baumeister, J. Lee, B. Yeom, J. H. Bahng, J. Lee, A. Violi and N. A. Kotov, *ACS Nano*, 2016, **10**, 1744–1755.
36 Y. Zhou, W. Wei, F. Cui, Z. Yan, Y. Sun, J. Ren and X. Qu, *Chem. Sci.*, 2020, **11**, 11344–11350.
37 S. Srivastava, A. Santos, K. Critchley, K.-S. Kim, P. Podsiadlo, K. Sun, J. Lee, C. Xu, G. D. Lilly, S. C. Glotzer and N. A. Kotov, *Science*, 2010, **327**, 1355–1359.
38 J. Han, H. Gong, X. Ren and X. Yan, *Nano Today*, 2021, **41**, 101295.
39 Z. Bian, K. Kato, T. Ogoshi, Z. Cui, B. Sa, Y. Tsutsui, S. Seki and M. Suda, *Adv. Sci.*, 2022, **9**, 2201063.
40 H. Wang, H. Yuan, S. Sae Hong, Y. Li and Y. Cui, *Chem. Soc. Rev.*, 2015, **44**, 2664–2680.
41 C. Hao, G. Wang, C. Chen, J. Xu, C. Xu, H. Kuang and L. Xu, *Nano-Micro Lett.*, 2023, **15**, 39.
42 S. Lee, C. Fan, A. Movsesyan, J. Bürger, F. J. Wendisch, L. de, S. Menezes, S. A. Maier, H. Ren, T. Liedl, L. V. Besteiro, A. O. Govorov and E. Cortés, *Angew. Chem., Int. Ed.*, 2024, **63**, e202319920.
43 X. Wen, S. Wang, R. Liu, R. Duan, S. Hu, T. Jiao, L. Zhang and M. Liu, *Small*, 2022, **18**, 2104301.
44 H.-E. Lee, R. M. Kim, H.-Y. Ahn, Y. Y. Lee, G. H. Byun, S. W. Im, J. Mun, J. Rho and K. T. Nam, *Nat. Commun.*, 2020, **11**, 263.
45 K. Saito, Y. Nemoto and Y. Ishikawa, *Nano Lett.*, 2024, **24**, 12840–12848.
46 Z. Zhang, H. Wang, T. Wu, G. Wang and F. Bai, *Small*, 2025, e09854.
47 L. Tan, W. Fu, Q. Gao and P. Wang, *Adv. Mater.*, 2024, **36**, 2309033.
48 L. Sun, Y. Tao, G. Yang, C. Liu, X. Sun and Q. Zhang, *Adv. Mater.*, 2025, **37**, 2306297.
49 J. Lu, Y. Xue, K. Bernardino, N.-N. Zhang, W. R. Gomes, N. S. Ramesar, S. Liu, Z. Hu, T. Sun, A. F. de Moura, N. A. Kotov and K. Liu, *Science*, 2021, **371**, 1368–1374.
50 X. Yue, L. Xu, H. Lin, C. Xu and S. Li, *Sci. Bull.*, 2023, **68**, 1764–1771.
51 Q. Guo, M. Zhang, Z. Tong, S. Zhao, Y. Zhou, Y. Wang, S. Jin, J. Zhang, H.-B. Yao, M. Zhu and T. Zhuang, *J. Am. Chem. Soc.*, 2023, **145**, 4246–4253.

52 Y. Zhou, Q. Ji, M. Masuda, S. Kamiya and T. Shimizu, *Chem. Mater.*, 2006, **18**, 403–406.
53 C. Wang, S. R. Mouchet, O. Deparis, J. Li, E. Paineau, D. Dragoe, H. Remita and M. N. Ghazzal, *Small*, 2024, **20**, 2402211.
54 Y. Negrín-Montecelo, A. Movsesyan, J. Gao, S. Burger, Z. M. Wang, S. Nlate, E. Pouget, R. Oda, M. Comesaña-Hermo, A. O. Govorov and M. A. Correa-Duarte, *J. Am. Chem. Soc.*, 2022, **144**, 1663–1671.
55 Y. Zheng, L. Lin, X. Ye, F. Guo and X. Wang, *Angew. Chem., Int. Ed.*, 2014, **53**, 11926–11930.
56 R. A. Callahan, D. C. Coffey, D. Chen, N. A. Clark, G. Rumbles and D. M. Walba, *ACS Appl. Mater. Interfaces*, 2014, **6**, 4823–4830.
57 G. Ghosh, M. Paul, T. Sakurai, W. Matsuda, S. Seki and S. Ghosh, *Chem. – Eur. J.*, 2018, **24**, 1938–1946.
58 A. Saeki, S. Seki, T. Sunagawa, K. Ushida and S. Tagawa, *Philos. Mag.*, 2006, **86**, 1261–1276.
59 A. Saeki, S. Seki, Y. Koizumi and S. Tagawa, *J. Photochem. Photobiol. A Chem.*, 2007, **186**, 158–165.
60 A. Saeki, Y. Koizumi, T. Aida and S. Seki, *Acc. Chem. Res.*, 2012, **45**, 1193–1202.
61 J. A. Schellman and P. Oriel, *J. Chem. Phys.*, 1962, **37**, 2114–2124.
62 J. Kwon, K. H. Park, W. J. Choi, N. A. Kotov and J. Yeom, *Acc. Chem. Res.*, 2023, **56**, 1359–1372.
63 P. J. Stephens, *Annu. Rev. Phys. Chem.*, 1974, **25**, 201–232.
64 W. R. Mason, *A Practical Guide to Magnetic Circular Dichroism Spectroscopy*, John Wiley & Sons, Ltd, 2007, pp. 14–35.
65 B. Han, X. Gao, J. Lv and Z. Tang, *Adv. Mater.*, 2020, **32**, 1–16.
66 Y. R. Weng, Y. Qin, Y. Ai, X. G. Chen, X. J. Song, H. Y. Zhang and W. Q. Liao, *Angew. Chem., Int. Ed.*, 2025, **64**, e202515806.
67 W. J. Choi, G. Cheng, Z. Huang, S. Zhang, T. B. Norris and N. A. Kotov, *Nat. Mater.*, 2019, **18**, 820–826.
68 X. Chen, H. Wang, C. Wang, C. Ouyang, G. Wei, T. Nie, W. Zhao, J. Miao, Y. Li, L. Wang and X. Wu, *Adv. Photonics Res.*, 2021, **2**, 1–10.
69 A. N. Nair, S. Fernandez, M. Marcos-Hernández, D. R. Romo, S. R. Singamaneni, D. Villagran and S. T. Sreenivasan, *Nano Lett.*, 2023, **23**, 9042–9049.
70 Y. Lu, Q. Wang, R. He, F. Zhou, X. Yang, D. Wang, H. Cao, W. He, F. Pan, Z. Yang and C. Song, *Angew. Chem., Int. Ed.*, 2021, **60**, 23578–23583.
71 A. Stefani, T. Salzillo, P. R. Mussini, T. Benincori, M. Innocenti, L. Pasquali, A. C. Jones, S. Mishra and C. Fontanesi, *Adv. Funct. Mater.*, 2024, **34**, 2308948.
72 J. Labella, D. K. Bhowmick, A. Kumar, R. Naaman and T. Torres, *Chem. Sci.*, 2023, **14**, 4273–4277.
73 K. Ray, S. P. Ananthavel, D. H. Waldeck and R. Naaman, *Science*, 1999, **283**, 814–816.
74 B. Göhler, V. Hamelbeck, T. Z. Markus, M. Kettner, G. F. Hanne, Z. Vager, R. Naaman and H. Zacharias, *Science*, 2011, **331**, 894–897.
75 R. Naaman and D. H. Waldeck, *J. Phys. Chem. Lett.*, 2012, **3**, 2178–2187.
76 H. Inui, A. Fujii, K. Tanaka, H. Sakamoto and K. Ishizuka, *Acta Crystallogr., Sect. B*, 2003, **59**, 802–810.
77 Y. Ma, P. Oleynikov and O. Terasaki, *Nat. Mater.*, 2017, **16**, 755–759.
78 Y. Zhou, Z. Dong, O. Terasaki and Y. Ma, *Acc. Mater. Res.*, 2022, **3**, 110–121.
79 T. Ohsuna, Z. Liu, S. Che and O. Terasaki, *Small*, 2005, **1**, 233–237.
80 A. Winkelmann and G. Nolze, *Ultramicroscopy*, 2015, **149**, 58–63.
81 R. Juchtmans, A. Béché, A. Abakumov, M. Batuk and J. Verbeeck, *Phys. Rev. B:Condens. Matter Mater. Phys.*, 2015, **91**, 94112.
82 D. Morikawa, K. Shibata, N. Kanazawa, X. Z. Yu and Y. Tokura, *Phys. Rev. B:Condens. Matter Mater. Phys.*, 2013, **88**, 24408.
83 T. Duan, J. Ai, X. Cui, X. Feng, Y. Duan, L. Han, J. Jiang and S. Che, *Chem*, 2021, **7**, 2695–2707.
84 Y. Duan, L. Han, J. Zhang, S. Asahina, Z. Huang, L. Shi, B. Wang, Y. Cao, Y. Yao, L. Ma, C. Wang, R. K. Dukor, L. Sun, C. Jiang, Z. Tang, L. A. Nafie and S. Che, *Angew. Chem., Int. Ed.*, 2015, **54**, 15170–15175.
85 D. Viladot, M. Véron, M. Gemmi, F. Peiró, J. Portillo, S. Estradé, J. Mendoza, N. Llorca-Isern and S. Nicolopoulos, *J. Microsc.*, 2013, **252**, 23–34.
86 P. Sutter, S. Wimer and E. Sutter, *Nature*, 2019, **570**, 354–357.
87 R. Erni, M. D. Rossell, C. Kisielowski and U. Dahmen, *Phys. Rev. Lett.*, 2009, **102**, 96101.
88 Z. Dong and Y. Ma, *Nat. Commun.*, 2020, **11**, 1588.
89 J. Hu, Z. Dong, C. Chu and Y. Ma, *Nat. Chem.*, 2025, **17**, 1819–1825.
90 H. Im, S. Ma, H. Lee, J. Park, Y. S. Park, J. Yun, J. Lee, S. Moon and J. Moon, *Energy Environ. Sci.*, 2023, **16**, 1187–1199.
91 J. Cai, W. Zhang, L. Xu, C. Hao, W. Ma, M. Sun, X. Wu, X. Qin, F. M. Colombari, A. F. de Moura, J. Xu, M. C. Silva, E. B. Carneiro-Neto, W. R. Gomes, R. A. L. Vallée, E. C. Pereira, X. Liu, C. Xu, R. Klajn, N. A. Kotov and H. Kuang, *Nat. Nanotechnol.*, 2022, **17**, 408–416.
92 T. Luo, H. Li, Z. Zhang, S. Wang, X. Pan, S. Mourdikoudis, C. Xue, J. Li, K.-Y. Wong and G. Zheng, *Adv. Sci.*, 2025, **12**, 2502848.
93 W. Liu, X. Fang, X. Ju, K. Gao, D. Wang, H. Xu and J. Wang, *J. Colloid Interface Sci.*, 2024, **675**, 74–83.
94 X. Wang, K. Maeda, A. Thomas, K. Takanabe, G. Xin, J. M. Carlsson, K. Domen and M. Antonietti, *Nat. Mater.*, 2009, **8**, 76–80.
95 G. Liao, Y. Gong, L. Zhang, H. Gao, G.-J. Yang and B. Fang, *Energy Environ. Sci.*, 2019, **12**, 2080–2147.
96 W. J. Ong, L. L. Tan, Y. H. Ng, S. T. Yong and S. P. Chai, *Chem. Rev.*, 2016, **116**, 7159–7329.
97 S. N. Talapaneni, G. Singh, I. Y. Kim, K. AlBahily, A. H. Al-Muhtaseb, A. S. Karakoti, E. Tavakkoli and A. Vinu, *Adv. Mater.*, 2020, **32**, 1904635.
98 X. Chu, C. I. Sathish, J.-H. Yang, X. Guan, X. Zhang, L. Qiao, K. Domen, S. Wang, A. Vinu and J. Yi, *Small*, 2023, **19**, 2302875.

99 G.-Q. Zhao, Q.-E. Zhang, Y.-X. Xin, H.-Q. Lv, Y. Pan, C.-C. Hu, A.-L. Yu, L.-H. Li, L. Lu and J.-G. Yu, *Coord. Chem. Rev.*, 2026, **547**, 217144.
100 X. Ding, Q. Wang, H. Liu, J. Wang, P. Yan, H. Chen, P. Sun, X. Zhu, Z. Mo and H. Xu, *Int. J. Hydrogen Energy*, 2025, **187**, 152004.
101 J. Wang and S. Wang, *Coord. Chem. Rev.*, 2022, **453**, 214338.
102 D. Mottammal, J. Cherusseri, S. A. Thomas, R. Isaac, D. N. Rajendran and M. Y. Choi, *Adv. Mater. Technol.*, 2025, **10**, e00667.
103 W. Lin, W. Hong, L. Sun, D. Yu, D. Yu and X. Chen, *ChemSusChem*, 2018, **11**, 114–119.
104 X. Zhou, W. Miao, L. Xu, J. Luo, X. Fan, X. Ning, X. Zhou and X. Zhou, *Chem. – Eur. J.*, 2024, **30**, e202402665.
105 G. D. Gesesse, C. Li, E. Paineau, Y. Habibi, H. Remita, C. Colbeau-Justin and M. N. Ghazzal, *Chem. Mater.*, 2019, **31**, 4851–4863.
106 T. Wang, Y. Li, W.-T. Wu, Y. Zhang, L. Wu and H. Chen, *Appl. Surf. Sci.*, 2021, **537**, 148025.
107 C. Wang, J. Li, E. Paineau, H. Remita and M. N. Ghazzal, *Sol. RRL*, 2023, **7**, 2200929.
108 W. Ma, J. Mao, C. Hao, L. Xu, C. Xu and H. Kuang, *Appl. Catal., B*, 2019, **245**, 691–697.
109 J. F. Qian, H. D. Yue, P. X. Qiu, Q. Liang, M. T. Hang, M. Y. He, Y. F. Bu, Q. Chen and Z. H. Zhang, *J. Solid State Chem.*, 2021, **304**, 122632.
110 W. Weng and J. Guo, *Nat. Commun.*, 2022, **13**, 5768.
111 S. H. Yang, R. Naaman, Y. Paltiel and S. S. P. Parkin, *Nat. Rev. Phys.*, 2021, **3**, 328–343.
112 H. Li, Q. Quan, C.-Y. Wong and J. C. Ho, *Adv. Energy Sustainable Res.*, 2025, **6**, 2400326.
113 W. Mtangi, F. Tassinari, K. Vankayala, A. Vargas Jentzsch, B. Adelizzi, A. R. A. Palmans, C. Fontanesi, E. W. Meijer and R. Naaman, *J. Am. Chem. Soc.*, 2017, **139**, 2794–2798.
114 K. B. Ghosh, W. Zhang, F. Tassinari, Y. Mastai, O. Lidor-Shalev, R. Naaman, P. Möllers, D. Nürenberg, H. Zacharias, J. Wei, E. Wierzbinski and D. H. Waldeck, *J. Phys. Chem. C*, 2019, **123**, 3024–3031.
115 S. Ghosh, B. P. Bloom, Y. Lu, D. Lamont and D. H. Waldeck, *J. Phys. Chem. C*, 2020, **124**, 22610–22618.
116 W. Zhang, W. Wang, Y. Hu, H. Guan and L. Hao, *Int. J. Hydrogen Energy*, 2021, **46**, 3504–3509.
117 P. K. Bhartiya, M. Srivastava and D. Mishra, *Int. J. Hydrogen Energy*, 2022, **47**, 42160–42170.
118 C. Xiao, W. Fu, L. Tan and P. Wang, *Adv. Funct. Mater.*, 2025, **35**, 2508134.
119 S.-J. Zheng, H. Chen, S.-Q. Zang and J. Cai, *Matter*, 2025, **8**, 101924.
120 Y. Wu, L. Cheng, Y. Tang, H. Sun and Q. Xiang, *Adv. Funct. Mater.*, 2025, e16617.
121 R. Naaman, Y. Paltiel and D. H. Waldeck, *Nat. Rev. Chem.*, 2019, **3**, 250–260.
122 X. Bai, Y. Cao, Y. Xu, W. Huang, P. Deng, X. Tian, Z. Liu, J. Wang and J. Tu, *ChemPhysChem*, 2022, **23**, e202200156.
123 W. Zhang, H. Guan, C. Kuang, W. Wang, Y. Hu and X. Yang, *Mater. Lett.*, 2022, **308**, 131130.
124 X. Kong, J. Ke, Z. Wang, Y. Liu, Y. Wang, W. Zhou, Z. Yang, W. Yan, Z. Geng and J. Zeng, *Appl. Catal., B*, 2021, **290**, 120067.
125 L. Pan, M. Ai, C. Huang, L. Yin, X. Liu, R. Zhang, S. Wang, Z. Jiang, X. Zhang, J. J. Zou and W. Mi, *Nat. Commun.*, 2020, **11**, 418.
126 Y. Li, Z. Wang, Y. Wang, A. Kovács, C. Foo, R. E. Dunin-Borkowski, Y. Lu, R. A. Taylor, C. Wu and S. C. E. Tsang, *Energy Environ. Sci.*, 2022, **15**, 265–277.
127 P. Saha, S. Amanullah and A. Dey, *Acc. Chem. Res.*, 2022, **55**, 134–144.
128 Y. Lang, D. Hong, R. Ma, H. Zhang, L. Xu, X. Zhao, D. Wu, Y. Li, D. Zhou, Z. Song, Y. Wen, Y. Yang, J. Han and J. Qiu, *J. Colloid Interface Sci.*, 2025, **699**, 138262.
129 C.-C. Lin, S.-K. Huang, W.-N. Tseng, C.-J. Su, C.-C. Huang, C.-Y. Huang, C.-Y. Yu, M.-H. Lai, J.-Y. Sun, Y.-C. Chao, H.-S. Hsu, C.-W. Luo, Y.-M. Chang, C.-C. Chen and C.-W. Chen, *J. Am. Chem. Soc.*, 2025, **147**, 40347–40355.
130 P. Yan, Q. Wang, J. Wang, H. Xu, J. Yang, Y. Zhu, Q. Chen, H. Mei and Y. Xu, *Chem. Eng. J.*, 2025, **507**, 160789.
131 Y. Cui, J. Ai, Y. Duan, M. Jia, T. Ouyang, A. Liu, L. Yu, J. Liu, X. Liu, C. Chu, Y. Li, Y. Ma, L. Chen, L. Han, J. Chen, C. Tian, S. Che and Y. Fang, *Chem*, 2025, **11**, 102390.
132 A. J. Medford and M. C. Hatzell, *ACS Catal.*, 2017, **7**, 2624–2643.
133 K. A. Brown, D. F. Harris, M. B. Wilker, A. Rasmussen, N. Khadka, H. Hamby, S. Keable, G. Dukovic, J. W. Peters, L. C. Seefeldt and P. W. King, *Science*, 2016, **352**, 448–450.
134 R. R. Eady, *Chem. Rev.*, 1996, **96**, 3013–3030.
135 J. M. Smith, A. R. Sadique, T. R. Cundari, K. R. Rodgers, G. Lukat-Rodgers, R. J. Lachicotte, C. J. Flaschenriem, J. Vela and P. L. Holland, *J. Am. Chem. Soc.*, 2006, **128**, 756–769.
136 K. Zhu, Y. Ju, J. Xu, Z. Yang, S. Gao and Y. Hou, *Acc. Chem. Res.*, 2018, **51**, 404–413.
137 S. Wang, J. Xu, W. Li, S. Sun, S. Gao and Y. Hou, *Chem. Rev.*, 2022, **122**, 5411–5475.
138 G. F. Chen, Y. Yuan, H. Jiang, S. Y. Ren, L. X. Ding, L. Ma, T. Wu, J. Lu and H. Wang, *Nat. Energy*, 2020, **5**, 605–613.
139 F. Y. Chen, Z. Y. Wu, S. Gupta, D. J. Rivera, S. V. Lambeets, S. Pecaut, J. Y. T. Kim, P. Zhu, Y. Z. Finfrock, D. M. Meira, G. King, G. Gao, W. Xu, D. A. Cullen, H. Zhou, Y. Han, D. E. Perea, C. L. Muhich and H. Wang, *Nat. Nanotechnol.*, 2022, **17**, 759–767.
140 P. H. van Langevelde, I. Katsounaros and M. T. M. Koper, *Joule*, 2021, **5**, 290–294.
141 M. Duca and M. T. M. Koper, *Energy Environ. Sci.*, 2012, **5**, 9726–9742.
142 Y. Wang, C. Wang, M. Li, Y. Yu and B. Zhang, *Chem. Soc. Rev.*, 2021, **50**, 6720–6733.
143 Q. Wang, J. Liu, S. Li, S. Ji, C. Zhang, J. Wang, J. Zhang and Y. Wang, *Angew. Chem., Int. Ed.*, 2025, e202517047.
144 X. Meng, C. Qin, X. L. Wang, Z. M. Su, B. Li and Q. H. Yang, *Dalton Trans.*, 2011, **40**, 9964–9966.

145 X. Yue, S. Li, H. Lin, C. Xu and L. Xu, *Adv. Funct. Mater.*, 2023, **33**, 2210046.
146 Y. N. Zhang, W. Dai, Y. Wen and G. Zhao, *Appl. Catal., B*, 2017, **212**, 185–192.
147 C. Li, E. Paineau, F. Brisset, S. Franger, C. Colbeau-Justin and M. N. Ghazzal, *Catal. Today*, 2019, **335**, 409–417.
148 S. Ma, H. Lee and J. Moon, *Adv. Mater.*, 2024, **36**, 2405685.
149 B. P. Bloom, Y. Paltiel, R. Naaman and D. H. Waldeck, *Chem. Rev.*, 2024, **124**, 1950–1991.
150 Y. Dong, A. McConnell, M. P. Hautzinger, M. A. Haque, A. H. Comstock, P. M. Theiler, J. M. Luther, P. C. Sercel, D. Sun and M. C. Beard, *Science*, 2025, **390**, 595–600.
151 S. Wadhwa, D. Buyens and J. G. Korvink, *Adv. Mater.*, 2024, **36**, 2408547.
152 R. Penasa, G. Licini and C. Zonta, *Chem. Soc. Rev.*, 2025, **54**, 10940–10955.
153 J. Cheng, X. Hong, X. Zu, W. Liu and D. Deng, *Photon Sci.*, 2025, DOI: 10.1021/photonsci.5c00018.